

# Luminosity distance uncertainties from gravitational wave detections of binary neutron stars by third generation observatories

Josiel Mendonça Soares de Souza

*Departamento de Física Teórica e Experimental,*

*Universidade Federal do Rio Grande do Norte, Natal-RN 59072-970, Brazil\**

Riccardo Sturani

*Instituto de Física Teórica, UNESP-Universidade Estadual Paulista & ICTP South*

*American Institute for Fundamental Research, São Paulo 01140-070, SP, Brazil†*

A new generation of terrestrial gravitational wave detectors is currently being planned for the next decade, and it is expected to detect most of the coalescences of compact objects in the universe with masses up to a thousand times the solar mass. Among the several possible applications of current and future detections, we focus on the impact on the measure of the luminosity distance of the sources, which is an invaluable tool for constraining the cosmic expansion history of the universe.

We study two specific detector topologies, triangular and  $L$ -shaped, by investigating how topology and relative orientation of up to three detectors can minimize the uncertainty measure of the luminosity distance. While the precision in distance measurement is correlated with several geometric angles determining the source position and orientation, focusing on bright standard sirens and assuming redshift to be measured with high accuracy, we obtain analytic and numerical results for its uncertainty depending on type and number of detectors composing a network, as well as on the inclination angle of the binary plane with respect to the wave propagation direction. We also analyze the best relative location and orientation of two third generation detectors to minimize luminosity distance uncertainty, showing that prior knowledge of the inclination angle distribution plays an important role in precision recovery of luminosity distance, and that a suitably arranged network of detectors can reduce drastically the uncertainty measure, approaching the limit imposed by lensing effects intervening between source and detector at redshift  $z \gtrsim 0.7$ .

## I. INTRODUCTION

While still in its infancy, gravitational wave (GW) astronomy is already providing observational data [1–3] of invaluable importance also for testing the fundamental nature of gravity [4, 5] and cosmology [6–8].

Second generation (2G) detectors LIGO [9] and Virgo [10] collected signals from coalescing binaries at the rate of  $O(1)$  event per week during their third observation run, and a similar or large rate is expected for future observations runs to happen presently or in the near future [11], when the Japanese detector KAGRA will also be part of the observational network [12].

The GW detections from coalescing binaries impacted on several fields in physics, and in this work we focus on the determination of the *luminosity distance* of their sources, which is a crucial ingredient to reconstruct the cosmic expansion history.

As well known [13, 14], coalescing binaries are *standard sirens*, i.e. their characteristic chirp signal enables an absolute calibration of the gravitational luminosity leading to an unbiased determination of the luminosity distance, which, together with redshift, are the two observables necessary to determine the cosmic expansion history of the universe. However redshift is in general not provided by GW detections, but it can be obtained by the host galaxy identification, which is possible for electromagnetically (EM) *bright* standard sirens. The most likely case, even though not exclusive, see e.g. [15–21], of GW signal accompanied by an EM counterpart is given by binary neutron star systems with mass ratio close to unity, for which tidal forces are larger [22]<sup>1</sup>. In the case the neutron star is tidally disrupted outside the effective innermost stable orbit of the binary, material is ejected from the system and it is expected to produce an EM counterpart [21], in particular a short gamma ray burst and a kilonova, beside lower frequency emission lasting up to years [21, 23].

For reference, GW-determined sky localisation areas encompassed  $\Delta\Omega$  of, say,  $\sim 16 - \text{few} \times 10^3 \text{ deg}^2$  in recent detections [1–3]. Up to a distance of 100 Mpc the number of galaxies  $N_{100}$  included in a sky region of area  $\Delta\Omega$  is roughly  $N_{100} \sim 5 \times \Delta\Omega / (10 \text{ deg}^2)$  assuming the average milky-way-like galaxy density to be  $\sim 5 \times 10^{-3} \text{ Mpc}^{-3}$  [24].

---

\*Electronic address: josiel.mendonca.064@ufrn.edu.br

†Electronic address: riccardo.sturani@unesp.br

<sup>1</sup> Tidal forces in the final stage of the inspiral they are inversely proportional to the (square) mass of the object sourcing the tidal field.

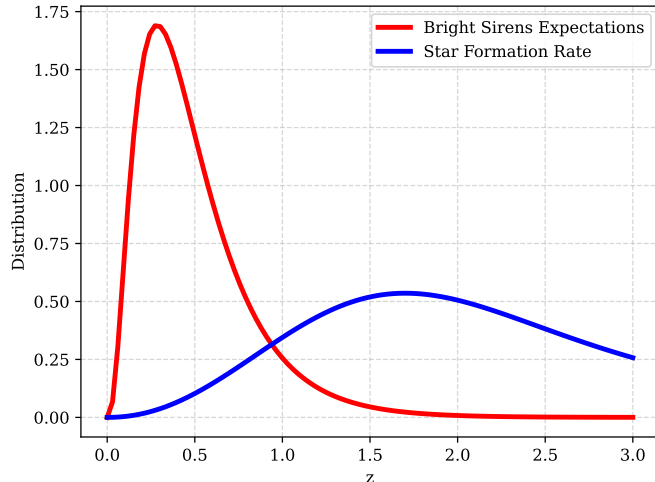


Figure 1: Expected redshift distribution of bright standard sirens assuming an electromagnetic counterpart is detected by Theseus [37], compared with observed star formation rate [40].

Events collected so far by 2G detectors show an overwhelming majority of binary black holes over binary systems involving at least one neutron star. In only one case, the notable binary neutron star (BNS) system that sourced GW170817 [25], the GW signal has been accompanied by EM counterparts, with consequent host galaxy identification and redshift determination. While several methods have been proposed and used to get redshift information from EM-dark GW detections, using e.g. statistical identification of host galaxy [26–28], full cross-correlating with galaxy catalogues [8, 29, 30], statistical redshift distribution of sources [31, 32], features in the black hole mass spectrum [33], neutron star tidal effects imprinted in the waveform [34], the golden events having the individually highest constraining power over the cosmic expansion history are EM-bright standard sirens, where host galaxy identification enable redshift determination with negligible error [35].

For third generation (3G) detectors most of the BNS coalescences will be visible [36], but EM counterparts are not expected to be detected beyond a limiting redshift  $\bar{z} \simeq 0.7$ , with the bulk of the distribution of bright standard sirens expected around  $z \sim 0.3 - 0.4$  [37, 38], making most of them invisible to 2G detectors [39], see Figure 1.

3G detectors are currently under active research and development, and in the present work we will assume that the Einstein Telescope (ET) will be a triangular interferometer

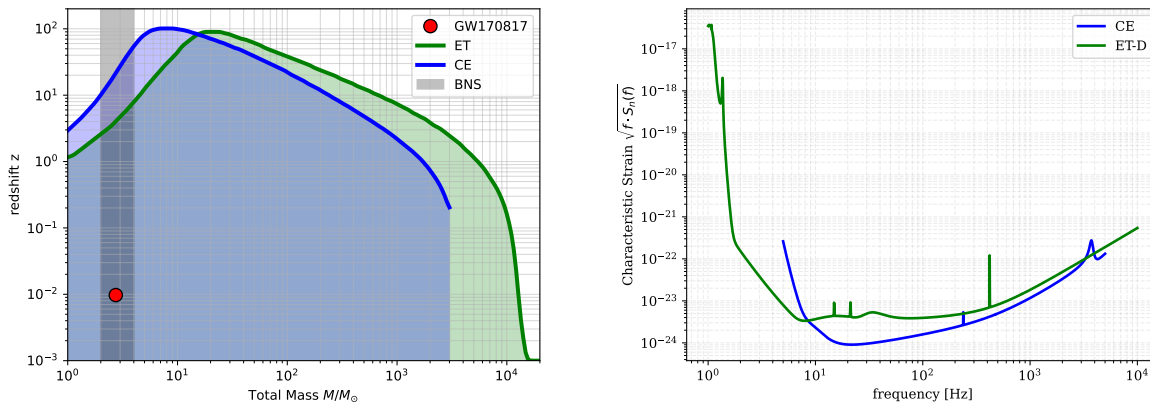


Figure 2: (Left) Luminosity distance reach for equal mass, non-spinning system, assuming fundamental  $l = m = 2$  mode only, for optimally oriented binaries, given the spectral noise density  $S_n$  [45, 46] for CE and [ET-D] from [47] for ET. The mass and luminosity distance of GW170817 are highlighted, as well as the mass region where BNSs are expected. (Right) Dimensionless noise characteristic strain  $h_c$ , defined in terms of spectral noise  $h_c \equiv \sqrt{f S_n}$  for  $L$ -shaped CE and triangle-shaped ET.

with arms at  $60^\circ$  degrees [41], and Cosmic Explorer (CE) a single  $L$ -shaped interferometer [42] with arms at  $90^\circ$ , with dimensionless noise characteristic strain  $h_c = \sqrt{f S_n}$  displayed in Figure 2,  $S_n$  being the standard single sided noise spectral density, see e.g. ch.7 of [43], while analogue quantities for 2G detectors can be found in [44].

Within this context we investigate the relative configuration of ET-like and CE-like detectors that maximizes the accuracy on the luminosity distance determination of binary neutron stars, taking into account statistical features of the sources like inclination angle distribution.

The paper is organised as follows. In Section II we lay out the tools employed to quantitatively analyze luminosity distance measures in EM-bright GW detections by the 3G detectors mentioned above, with the results presented in Section III. Section IV contains the conclusions that can be drawn from our study.

## II. METHOD

### A. Basics

Gravitational radiation in general relativity are endowed with two polarisations, conventionally indicated by  $h_+$  and  $h_\times$ , which can be suitably decomposed into modes using spin-weighted spherical harmonics  ${}^{-s}Y_{lm}$  of weight  $s = -2$ , according to

$$h_+ - ih_\times = \frac{GM}{r} \sum_{l \geq 2} \sum_{|m| \leq l} H_{lm} {}^{-2}Y_{lm}(\iota, \phi), \quad (1)$$

where Newton constant  $G$ , total rest mass  $M$  of the source, and coordinate distance of the source to the observer  $r$  have been factored out. The luminosity distance  $d_L$  is related to  $r$  and the redshift  $z$  via  $d_L = (1+z)r$ . Applying Equation (1) to the case of a binary system,  $\iota$  denotes the angle between the unit vector perpendicular to the binary plane  $\hat{L}$  and the radiation direction parameterized by the unit vector  $\hat{N}$ ,  $\phi$  parameterizes a rotation in the binary plane.

The expansion coefficients  $H_{lm}$  are complex functions of the intrinsic parameters and the retarded time  $t-r$ . Detector  $d_i$  output contain GW signals  $h_{d_i}$  which are linear combinations of the GW polarisations weighted by the *pattern functions*  $F_{+,\times}$

$$h_{d_i} = F_+(\alpha_i, \beta_i, \psi_i)h_+ + F_\times(\alpha_i, \beta_i, \psi_i)h_\times, \quad (2)$$

where  $\alpha_i, \beta_i$  are detector dependent angles determined by the sky position of the source, and the polarisation angles  $\psi_i$  can be interpreted as the additional angle (beside  $\iota$ ) relating  $\hat{L}$  to  $\hat{N}$  [48]. Together  $\psi_i, \iota$ , and  $\phi$  compose the *Euler angles* determining the relative orientation between *source frame* (defined by the orbital plane and its normal  $\hat{L}$ ) and the *radiation frame* whose  $\hat{z}_{rad}$  axis is the unit vector  $\hat{N}$ , and whose  $\hat{x}_{rad} - \hat{z}_{rad}$  plane contains the normal to the detector's plane  $\hat{z}_i$ , see Appendix A for detailed definition and properties of the polarisation angle.

The pattern functions  $F_{+,\times}$  can be written as

$$\begin{aligned} F_+(\alpha_i, \beta_i, \psi_i) &= \cos(2\psi_i)f_+(\alpha_i, \beta_i) - \sin(2\psi_i)f_\times(\alpha_i, \beta_i), \\ F_\times(\alpha_i, \beta_i, \psi_i) &= \cos(2\psi_i)f_\times(\alpha_i, \beta_i) + \sin(2\psi_i)f_+(\alpha_i, \beta_i), \end{aligned} \quad (3)$$

with  $f_{+,\times}$  defined as

$$\begin{aligned} f_+(\alpha_i, \beta_i) &\equiv -\sin(\Omega)\frac{1}{2}(1 + \cos^2\beta_i)\sin(2\alpha_i), \\ f_\times(\alpha_i, \beta_i) &\equiv -\sin(\Omega)\cos\beta_i\cos(2\alpha_i), \end{aligned} \quad (4)$$

where  $\beta_i$  is (the complement of) the source elevation and the azimuth angle  $\alpha_i$  is measured with respect to the bisector of the angle formed by the interferometer's arms. The pattern functions (4) can be obtained by projecting the gravitational perturbation tensor onto the interferometer response tensor  $\frac{1}{2}(u^i u^j - v^i v^j)$ , begin  $\hat{u}, \hat{v}$  the unit vector pointing along the detector's arms, and we allow the possibility of a variable opening angle  $\Omega$  between them, see Figure 3.<sup>2</sup>

As per standard treatment, the detectors' output  $h_{d_i}$  are processed via *matched-filtering* [49], which consists in taking a noise-weighted correlation of the data with a pre-computed waveform model, or *template*  $h_t$ , according to<sup>3</sup>

$$\langle h_{d_i}, h_{t_i} \rangle(t_i) \equiv 2 \int_0^\infty \frac{[\tilde{h}_{d_i}(f)\tilde{h}_{t_i}^*(f)e^{-2i\pi f t_i} + \tilde{h}_{d_i}^*(f)\tilde{h}_{t_i}(f)e^{2i\pi f t_i}]}{S_{n_i}(f)} df, \quad (5)$$

whose output is the time-dependent correlation between data and the specific template  $h_{t_i}$  translated in time by the detector dependent quantity  $t_i$ .  $S_n(f)$  is the noise spectral density defined in term of detector noise  $\tilde{n}(f)$  averaged over many realizations

$$\langle \tilde{n}(f)\tilde{n}(f') \rangle = \frac{1}{2}S_n(f)\delta(f + f'). \quad (6)$$

The correlation in Equation (5) can be used to define a scalar product  $\langle h_1|h_2 \rangle \equiv \langle h_1, h_2 \rangle(0)$  and consequently a norm  $\|h\| \equiv \sqrt{\langle h|h \rangle}$ .

Searches for maximum matched-filtering output by varying the templates lead to the determination of the best fit waveform and, in a Bayesian inference scheme, to probability distribution functions for all waveform template parameters. Note that the binary constituent masses  $m_i$  that can be recovered are the so-called *redshifted*, or *detector* ones, related to intrinsic, or source ones  $m_i^{(s)}$  via  $m_i = m_i^{(s)}(1 + z)$ [13]. Optimal matched-filtering leads to the definition of signal-to-noise ratio of signal  $h$  ( $SNR_h$ ):

$$SNR_h^2 \equiv \langle h|h \rangle = 4 \int_0^\infty \frac{|\tilde{h}(f)|^2}{S_n(f)} df. \quad (7)$$

Focusing on the fundamental mode, i.e. taking the contribution only from  $l = 2 = |m|$

<sup>2</sup> We understand the  $\Omega$  dependence in the notation of  $f_{+, \times}$ . For all applications we will use  $\Omega = \pi/2$  for  $L$ -shaped (CE-like) interferometers and  $\Omega = \pi/3$  for triangle-shaped (ET-like) ones.

<sup>3</sup> We adopt the convention  $\tilde{g}(f) = \int g(t)e^{2i\pi f t} dt$ .

in (1), the signal from the inspiral phase admits a simple analytic description:

$$\begin{aligned}\tilde{h}_+ &= \frac{(1 + \cos^2 \iota)}{2} h_0(f) e^{i\Phi_{gw}(f)}, \\ \tilde{h}_\times &= i \cos \iota h_0(f) e^{i\Phi_{gw}(f)},\end{aligned}\quad (8)$$

where for  $h_0(f)$  the analytic expression is known analytically for the inspiral in the *stationary phase approximation* [50]

$$h_{0insp}(f) \equiv \left(\frac{5}{24}\right)^{1/2} \pi^{-2/3} \frac{(GM_c)^{5/6} f^{-7/6}}{d_L}, \quad (9)$$

being  $M \equiv m_1 + m_2$ ,  $M_c \equiv \nu^{3/5} M$ ,  $\nu \equiv m_1 m_2 / M^2$ . Similarly the  $f$ -domain phase  $\Phi_{gw}(f)$  has a well known analytic, perturbative representation for the *inspiral* phase of the  $i$ -th detector:

$$\Phi_{gw_i-insp}(f) - 2\pi f t_i + \phi_0 + \frac{\pi}{4} \simeq \frac{3}{128\nu v^5} [1 + O(v^2)] = \frac{3}{128(\pi GM_c f)^{5/3}} [1 + O(v^2)], \quad (10)$$

where the quantity  $(\Phi_{gw_i-insp} - 2\pi f t_i)$  is independent of the detector ( $t_i$  is the arrival time at the  $i$ -th detector), the small parameter of expansion in Equation (10) is  $v \equiv (\pi GM f)^{1/3}$ , and  $\phi_0$  a constant phase.

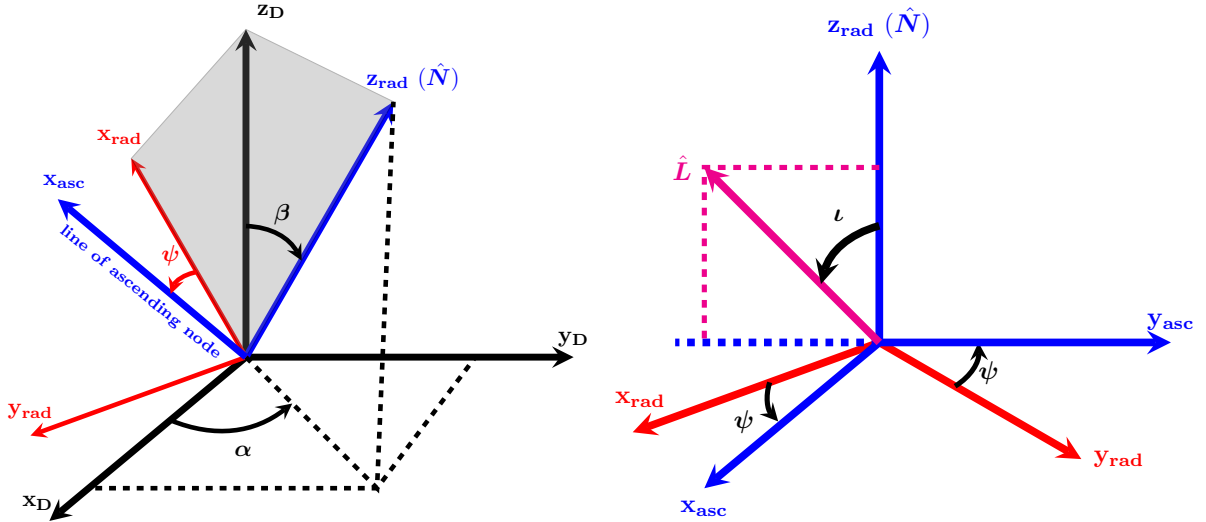


Figure 3: Schematic representation of detector geometry and of radiation frame.

Out of the 15 parameters needed to determine the signal imprinted into a detector by a GW source made of a binary system in circular motion, see Tab. I, we are interested in the precision of luminosity distance determination of EM bright standard sirens, for which we

Intrinsic parameters	Extrinsic parameters
$M_c, \nu, \vec{S}_1, \vec{S}_2$	$\mathbf{d}_L, \psi, \iota, \phi, \alpha, \beta, t$

Table I: Parameters defining the observation of a binary system observation (whose constituents are treated as point-like object), divided between intrinsic ( $\vec{S}_{1,2}$  are the binary constituent spin vectors) and extrinsic ( $t$  denotes the arrival time), according to the distinction introduced in [51]. In bold are those we searched over via Bayesian inference ( $d_L, \psi, \iota$ ), in grey the one marginalised over ( $\phi$ ).

assume that sky position, and consequently host galaxy and then redshift, can be determined with negligible uncertainty.

As explained in the introduction, we focus our analysis on equal mass binary neutron stars, which are obvious candidates (even if not exclusive) to produce GW signals with EM counterpart. We will make the additional simplifying assumptions that binary constituent spins can be neglected, as neutron stars in binaries are observed to have in general negligible spins, with values  $\lesssim 0.05m_i^2$  [52]. The remaining intrinsic parameters, the individual masses, are expected to be measured with sub-percent accuracy, as it happened for GW170817 [25],<sup>4</sup> and as confirmed in general by Fisher matrix analysis for 3G detectors [53]<sup>5</sup>.

Matched-filtering technique can provide a very accurate determination in general of the intrinsic parameters, in particular the chirp mass  $M_c$  can be determined with accuracy [54]

$$\frac{\delta M_c}{M_c} \sim \frac{1}{N_{cyc}} \times \frac{10}{SNR}, \quad (11)$$

where beside the factor  $SNR^{-1}$  usually obtained in a Fisher matrix approximation, one has a  $N_{cyc}^{-1}$  uncertainty decrease with increasing number of observed cycles  $N_{cyc}$  from the phase  $\Phi_{gw}$  dependence on  $M_c$ , and the numerical factor  $\sim 10$  is due to correlation with the other mass parameter  $\nu$  which enters Equation (10) beyond leading order.

We further neglect in our Bayesian inference search the arrival time  $t_i$ , which is usually obtained with  $\sim msec$  accuracy [2] and concentrate on the parameters that have larger correlation with the luminosity distance, hence have stronger impact on its recovery value

<sup>4</sup> For reference, the luminosity distance of GW170817 has been measured with  $\sim 20\%$  accuracy and it had a network  $SNR_{net}$ , i.e. the  $SNR$  summed over three detectors of  $SNR_{net} = (\sum_{i=1}^3 SNR_{d_i}^2)^{1/2} \sim 32$ .

<sup>5</sup> In particular in Fig. 13 of [53] it is shown that about 99% of binary neutron star detections by both 2G and 3G detectors will have individual masses accuracy below 0.1%.



precision.

Note that also calibration errors can affect the measure of luminosity distance, and a proxy for the threshold at which relative calibration error  $\Delta_c$  become comparable with statistical ones is  $\Delta_c \sim 1/SNR$  [55]. While GW signals from binary neutron stars can reach  $SNR$  of  $10^3$  in 3G detectors [56], the bulk of their distribution will lie at  $SNR \lesssim \text{few} \times 10$  [53]. For this reason, projecting to 3G detectors the Advanced LIGO systematic calibration error in the first half of the third observation run, estimated  $< 2\%$  [57], one can assume that calibration uncertainty should not affect the overwhelming majority of signals we are discussing.

According to Equation (2), detectors with different orientations measure different combinations of  $h_+$  and  $h_\times$ , hence in principle with two or more detectors it is possible to disentangle the  $\iota - d_L$  degeneracy. However the two LIGOs are oriented to have very similar pattern functions (apart from a sign) [58] and in the GW170817 case very little SNR was present in the remaining detector of the network, Virgo [25].

Another element that can break the degeneracy is the presence in the signal of a significant contribution from sub-dominant modes with  $l > 2$ , which are weighted by different function of  $\iota$  than the  $l = 2, |m| = 2$  mode determining Equation (8). However sub-dominant modes are not expected to be seen in GWs emitted by binary neutron stars, whose part of the signal visible in the detectors is in the inspiral phase<sup>6</sup> for which subdominant modes are suppressed by powers of the relative binary constituent velocity as  $v^{l-2}$ . Moreover odd higher modes vanish in the limit  $m_1 = m_2$ , hence they are suppressed for comparable masses and in general sub-dominant modes are more important for edge-on viewing angles, i.e.  $\iota \sim \pi/2$  [59]. We will come back on source  $\iota$  distribution in Subsection III B.

## B. Cutler-Flanagan parameterization

Crucial roles to estimate the luminosity distance measurement uncertainty are played by detector topology, location and orientation and we find convenient to investigate this issue using the parameterization of the signal introduced in [60]. For a single detector  $d_i$ , denoting

---

<sup>6</sup> For reference, the inner most stable circular orbit for a spin-less, equal mass binary system, corresponds to a GW frequency  $f_{GW} \simeq 730\text{Hz} [M / (3M_\odot)]^{-1}$ .

$v \equiv \cos \iota$ ,  $\chi_+ \equiv (1 + v^2)/2$  (and  $\chi_\times \equiv -iv$  for future reference) one can write the  $SNR$  as

$$\begin{aligned} SNR_i^2 &= 2 (f_{+i}^2 + f_{\times i}^2) \left\{ (\chi_+^2 + v^2) + (\chi_+^2 - v^2) \cos [4 (\psi_i + \bar{\psi}_i)] \right\} \int_0^\infty \frac{|h_0(f)|^2}{S_{n_i}(f)} df \\ &= 2 (f_{+i}^2 + f_{\times i}^2) (\chi_+^2 + v^2) [1 + f(v) \cos (4 (\psi_0 + \delta\psi_i + \bar{\psi}_i))] \int_0^\infty \frac{|h_0(f)|^2}{S_{n_i}(f)} df, \end{aligned} \quad (12)$$

where we have used the detector's output Equation (2) in the  $SNR$  expression (7). The newly introduced quantity  $\bar{\psi}_i$  is defined via

$$\cos (4\bar{\psi}_i) \equiv \frac{f_{+i}^2 - f_{\times i}^2}{f_{+i}^2 + f_{\times i}^2}, \quad \sin (4\bar{\psi}_i) \equiv \frac{2f_{+i}f_{\times i}}{f_{+i}^2 + f_{\times i}^2}, \quad (13)$$

and in the second line of Equation (12) we have written  $\psi_i = \psi_0 + \delta\psi_i$ , where  $\psi_0$  is the polarisation angle relative to the earth north pole unit vector  $\hat{z}_0$  (i.e. using  $\hat{z}_0$  for  $\hat{z}_i$  in Equation (A3),  $\delta\psi_i$  being defined as a consequence). Finally we adopted the notation

$$f(v) \equiv \frac{\chi_+^2 - v^2}{\chi_+^2 + v^2} = \frac{(1 - v^2)^2}{1 + 6v^2 + v^4}. \quad (14)$$

The pattern functions  $f_{+, \times i}$  depend on detector location via their arguments  $(\alpha_i, \beta_i)$  as per Equation (4),  $\delta\psi_i$  depends on the source location with respect to the detector but it has the non-trivial property of not depending on the polarisation angle, see Appendix A.

The main advantage of the  $SNR$  formulation in Equation (12) is that it separates the contribution to the  $SNR$  in a part that depends on the polarisation angle  $\psi$  and a part that is  $\psi$ -independent. In general it is difficult to recover  $\psi$  and its uncertainty affects the measure of the  $SNR$ , see Equation (21), hence jeopardizing the precision of  $d_L$ .

Given that the polarisation angle parameterizes rotations in the  $+, \times$  space, the signal in each detector can be elegantly written in terms of quadratic forms via

$$\begin{aligned} \tilde{h}_{d_i} &= h_0(f) e^{i\Phi_{gw_i}} V_A(v) R_{AB} (2\psi_0) R_{BC} (2\delta\psi_i) f_{C_i} \\ &= h_0(f) \mathcal{A}_A R_{AB} (2\delta\psi_i) f_{B_i} e^{2\pi i f t_i} \end{aligned} \quad (15)$$

where capital Latin indices  $A, B, C$  run over  $\{+, \times\}$ ,  $R_{AB}$  is the standard  $2 \times 2$  rotation matrix

$$R_{AB}(\alpha) \equiv \begin{pmatrix} \cos \alpha & -\sin \alpha \\ \sin \alpha & \cos \alpha \end{pmatrix}, \quad (16)$$

we have collected in a 2-vector the dependence of the GW polarisations on  $\iota$ , i.e.  $V_A(v) \equiv (\chi_+, \chi_\times)$ , and in the second line of Equation (15) we have defined the detector independent

quantity  $\mathcal{A}_A(v, \psi_0) \equiv V_B(v)R_{BA}(2\psi_0)e^{i\Phi_{gw}}$ . The rationale of this parameterization is to separate parameters which for a given signal are common to all detectors ( $h_0(f)\mathcal{A}_A$ ), from those depending on the detector  $R_{AB}(2\delta\psi_i)f_{Bi}e^{2\pi if t_i}$ .

Following [54], it is possible to generalize the  $SNR$  parameterization of Equation (12) to the case of a network made of  $n_{det}$  detectors

$$\begin{aligned} SNR_{net}^2 &\equiv \sum_{i=1}^{n_{det}} SNR_i^2 \\ &= SNR_0^2 \mathcal{R}eal[\mathcal{A}_A^*(v, \psi_0)\mathcal{A}_B(v, \psi_0)] \sum_{i=1}^{n_{det}} \Xi_{ABi}, \end{aligned} \quad (17)$$

with

$$\begin{aligned} \Xi_{ABi} &\equiv R_{AC}(2\delta\psi_i)R_{BD}(2\delta\psi_i)f_{Ci}f_{Di}\omega_i, \\ \omega_i &\equiv \frac{\int_0^\infty |h_0(f)|^2 S_{n_i}^{-1}(f) df}{\int_0^\infty |h_0(f)|^2 S_{n_{avg}}^{-1}(f) df}, \\ SNR_0^2 &\equiv 4 \int_0^\infty df \frac{|h_0(f)|^2}{S_{n_{avg}}(f)}, \\ S_{n_{avg}}^{-1}(f) &\equiv \frac{1}{n_{det}} \sum_i S_{n_i}^{-1}(f). \end{aligned} \quad (18)$$

One can then define a symmetric  $2 \times 2$  matrix  $\Xi_{AB}$ , which can be diagonalized by a suitable rotation matrix of the type (16) with angle  $\bar{\psi}$ , as:

$$\Xi_{AB} \equiv \sum_i \Xi_{ABi} = \sum_i R_{AC}(2\bar{\psi})\bar{\Xi}_{CD}R_{DB}(2\bar{\psi}), \quad (19)$$

whose explicit expression is reported in Appendix A, and it is convenient to parameterize the two degrees of freedom of diagonal matrix  $\bar{\Xi}_{AB}$  as

$$\bar{\Xi}_{AB} = \sigma \begin{pmatrix} 1 + \epsilon & 0 \\ 0 & 1 - \epsilon \end{pmatrix} \quad (20)$$

with  $\sigma = \frac{1}{2}(\Xi_{++} + \Xi_{\times\times})$  and  $\epsilon = \sqrt{(\Xi_{++} - \Xi_{\times\times})^2 + 4\Xi_{+\times}^2} / (\Xi_{++} + \Xi_{\times\times})$ , which is bounded by  $0 \leq \epsilon \leq 1$ . In the particular case of a single detector one has that  $\epsilon = 1$  (and  $\omega_1 = 1$ ), as each  $\Xi_{ABi}$  has vanishing determinant, being the outer product of two copies of the same vector.

For a generic detector network, the combined  $SNR_{net}^2$  of Equation (17) can then be written as

$$\begin{aligned} SNR_{net}^2 &= SNR_0^2 \mathcal{R}eal[\mathcal{A}_C^* R_{CA}(2\bar{\psi})\bar{\Xi}_{AB}R_{BD}(2\bar{\psi})\mathcal{A}_D] \\ &= SNR_0^2 \sigma [(\chi_+^2 + v^2) + \epsilon(\chi_+^2 - v^2) \cos(4(\psi_0 + \bar{\psi}))]. \end{aligned} \quad (21)$$

The quantities  $\sigma, \epsilon$  depends on the detector network and on the direction of propagation  $\hat{N}$ , but they are independent of other angles parameterizing the binary plane orientation  $(\iota, \psi, \phi)$ . For a fixed detector configuration  $\epsilon, \sigma$  parameterize in a simple way the  $SNR$  dependence which respectively depend and does not depend on the polarisation angle  $\psi$ . Note that an analogue but not equivalent parameterization has been introduced in [61], whose parameterization allows to pinpoint the *dominant polarisation* mode, i.e. the combination of polarizations that contributes the most to the  $SNR$ , see Appendix C.

### C. Expected rates

For cosmological applications it is crucial to have an accurate measure of the luminosity distance, which one can expect to be obtained by using multiple observatories sensitive to different polarisation combinations. The rate of EM bright standard siren is not supposed to exceed  $O(1)$  per year with current generation detectors [11], estimate for 3G detectors can lead to  $O(100)$  per year [37]. As for the expected redshift distribution, an example for EM-bright standard sirens is reported in Figure 1, where as a reference is also reported the star formation rate

$$R_{sfr} = \frac{1}{1+z} \frac{dV_c}{dz} \psi_{DM}(z), \quad (22)$$

where  $\psi_{DM}$  is the star formation rate taken from [40] and  $V_c$  is the comoving volume.<sup>7</sup>

In Figure 2 we report the luminosity distance reach of BNS for optimally oriented, equal mass, spin-less systems (i.e. the distance at which  $SNR_i = 8$ ) and the design noise curves of CE [42] and ET [62].

In the following Section we show non-trivial consequences that can be deduced from the parameterization in Equation (21), supporting them with numerical results obtained with Bayesian inference methods.

---

<sup>7</sup> Given the moderate range of expected bright standard sirens, our  $d_L$  recovery prior is uniform in comoving volume.

### III. RESULTS

#### A. The Bayesian setup

In a standard Bayesian inference framework one has to consider the likelihood

$$\mathcal{L} = e^{-\frac{1}{2} \sum_i \|h_{d_i} - h_{t_i}\|^2}, \quad (23)$$

where the norm has been inherited by the scalar product defined implicitly in Equation (5). We will consider the above likelihood for fixed values of the masses (setting the spins to zero), sky-position angles, and time of the event. This is a reasonable simplification of the problem, assuming that the EM counterpart allowed a precise sky localization, and that the correlation of the detected signal with long templates allowed a precise determination of the arrival time and the masses which determine the chirping phase of the signal.

By using only the dominant modes  $l = |m| = 2$ , one can cast the likelihood  $\mathcal{L}$  for data  $d_i$  into the form

$$\begin{aligned} \log \mathcal{L} &= - \sum_{i=1}^{n_{det}} \int_{-\infty}^{\infty} df \frac{|\tilde{h}_{d_i}(f) - \tilde{h}_{t_i}(f)|^2}{S_{n_i}(f)} \\ &= - \sum_{i=1}^{n_{det}} \int_{-\infty}^{\infty} \frac{df}{S_{n_i}(f)} \left[ |\tilde{h}_{d_i}(f)|^2 + |\tilde{h}_{t_i}(f)|^2 - 2\tilde{R}(f) \cos(2\phi) - 2\tilde{I}(f) \sin(2\phi) \right], \end{aligned} \quad (24)$$

where we have defined  $\tilde{R}(f), \tilde{I}(f)$  as, respectively, the real and imaginary part of  $\tilde{h}_{d_i}(f)\tilde{h}_{t_i}^*(f)$ .

Assuming a flat prior, marginalization over  $\phi$  can be performed analytically using [63, 64]

$$\frac{1}{2\pi} \int_0^{2\pi} dx e^{a \cos(x) + b \sin(x)} = I_0(\sqrt{a^2 + b^2}), \quad (25)$$

where  $I_\nu(x)$  is the Bessel function of the first kind of order  $\nu$ , and the marginalized likelihood  $\mathcal{L}_\phi$  will depend only on the extrinsic parameters  $d_L, \iota$  and  $\psi$ :

$$\mathcal{L}_\phi = \frac{1}{2\pi} \int_0^{2\pi} \mathcal{L} d\phi = \exp \left[ -\frac{1}{2} \sum_i^{n_{det}} (\|h_{d_i}\|^2 + \|h_{t_i}\|^2) \right] I_0 \left( 2 \left| \sum_i^{n_{det}} \int_{-\infty}^{\infty} df \frac{h_{d_i} h_{t_i}^*}{S_{n_i}(f)} \right| \right). \quad (26)$$

When considering the injection data to correlate with templates, we will work in the zero noise approximation [65], as usually done in literature to estimate average uncertainties in Gaussian noise.

We run `Bilby` [66] with the `Nestle` sampler [67], which implements the nested sampling algorithm [68], with 300 live points, searching over 3 parameters  $d_L, \psi, \iota$ . Results for every

$d_L$  injection are averaged over the 300 injections simulating random values of  $\alpha, \beta, \iota, \psi$ , which survives the  $SNR$  cutoff at 8 in each detector.

For simulation efficiency reason, we used *TaylorF2* waveform model [69] with fixed total mass  $M = 3M_\odot$ , equal binary component masses, no spins. We have also verified in a few cases that no significant deviations occur in the result when replaced with waveform complete with merger-ringdown model, like *IMRPhenomD* [70, 71], see right plot in Figure 17 for qualitative reference, and we neglected tidal effects.

### B. Impact of $\iota$ and source location on $d_L$ uncertainty

Expressions (20,21) permit to highlight the following fundamental features:

1. For a single detector  $\epsilon = 1$ ,  $\sigma = \frac{1}{2} (f_+^2 + f_\times^2)$  and we recover Equation (12) (and also Equation (A8) reduces to Equation (13)).
2. For co-located detectors and a source on the top of them one has  $f_+ = f_\times = \sin \Omega$ , implying  $\sigma = n_{det}/2 \times \sin^2 \Omega$ , which is its maximum value.
3. In the case of a single  $L$ -shaped detector ( $\epsilon = 1$ ), the detected signal is a single combination of the two polarisations and one has no information on the polarisation angle. Considering that for large argument the Bessel function has  $I_0(x) \sim e^x/\sqrt{2\pi x}$ , the marginalized likelihood can then be written as

$$\begin{aligned}
 -2 \log \mathcal{L}_\phi &= \sum_{i=1}^{n_{det}} (\|h_{d_i}\|^2 + \|h_{t_i}\|^2) - 2 \left[ x - \frac{1}{2} \log(2\pi x) \right], \\
 x &\equiv \left| \sum_{i=1}^{n_{det}} \int_{-\infty}^{\infty} \frac{h_{d_i} h_{t_i}^*}{S_{n_i}} df \right|,
 \end{aligned} \tag{27}$$

and the scalar product between data and template can be decomposed analogously to what done in Equation (17) for the SNR:

$$\langle h_{d_i} | h_{t_i} \rangle = SNR_0^2 \mathcal{R}eal \left[ \mathcal{A}_{d_i A}^* \mathcal{A}_{t B} \Xi_{dt_i AB} \right], \tag{28}$$

where  $\Xi_{dt_i AB} = R_{AC}(2\delta\psi_{d_i})R_{BD}(2\delta\psi_{t_i})f_C f_D \omega_i$  is the matched-filter analogue of the  $SNR$ -related quantity  $\Xi$  defined in (17), to which it reduces when the template equals the data. For a single detector ( $\omega_i = 1 = \epsilon$ , see Equations (18,19)) the matrix  $\Xi_{dt_i}$  is

not symmetric but can still be diagonalized into the form

$$\bar{\Xi}_{dt_i AB} = (F_+^2 + F_\times^2) \cos(2(\psi_{d_i} - \psi_{t_i})) \begin{pmatrix} 1 & 0 \\ 0 & 0 \end{pmatrix}, \quad (29)$$

each detector giving a contribution to the log-likelihood

$$\log \mathcal{L}_{i\phi} \propto 2\sigma \cos(2(\psi_{d_i} - \psi_{t_i})) (|\mathcal{A}_{d_i+}|^2 + |\mathcal{A}_{t_i+}|^2 - 2|\mathcal{A}_{d_i+}\mathcal{A}_{t_i+}|), \quad (30)$$

where here with  $+$ ,  $\times$  we denoted the ‘‘principal’’ polarisations diagonalizing  $\bar{\Xi}_{dt_i AB}$  (see Appendix A for the matrix diagonalising  $\bar{\Xi}_{dt_i AB}$ , and [72] for the version of Equation (30) not marginalized over  $\phi$ ). Equation (30) indicates that for  $\epsilon \sim 1$  the likelihood can constrain only one polarisation, leading to the well known bimodal degeneracy between  $v$  and  $d_L$ , as shown in top plots of Figure 4 for any value of the inclination angle sufficiently away from the  $\pi/2$  value.

For a network of interferometers things are qualitatively different as they are in general sensitive to more than one combination of the two GW-polarisations and  $\epsilon$  in Equation (20) can assume values between 0 and 1, depending on the source location, see Figure 5.

For instance for a triangle-shaped detector the condition  $\epsilon \sim 1$  is realized only by sources located in a small region of the sky corresponding to the blind (or almost blind) regions of the individual interferometer composing the triangle. They correspond to directions in the plane of the interferometers bisecting their arms, i.e.  $\alpha = \Omega/2$ ,  $\beta = \pi/2$  in Equation (4). See also Figure 6 and the additional material in Appendix B, showing that for a value of  $\epsilon \sim 1$  and a value of  $\iota$  sufficiently distant from the symmetric point  $\iota = \pi/2$ , bimodality appears in the  $d_L$ - $\iota$  2-dimensional probability distribution function (PDF). As expected, adding detectors into the network reduces the sizes of  $\epsilon \sim 1$  regions, see bottom of Figure 5.

4. It has been empirically noted, e.g. in [72, 74] where sky position is fixed, and [75] where sky localization angles are among the parameters searched for in the Bayesian inference, that for  $\iota \sim \pi/2$  the uncertainty in  $d_L$  usually drops for triangle-shaped detector, see Figure 7. Note that the drop in uncertainty while varying  $\iota$  at fixed redshift for the triangle-shaped detector is not due to an increase in  $SNR$ , which rather *decreases* as  $\iota \rightarrow \pi/2$ , as shown in Figure 8. Actually, it is due to  $v \rightarrow 0$ , leading to

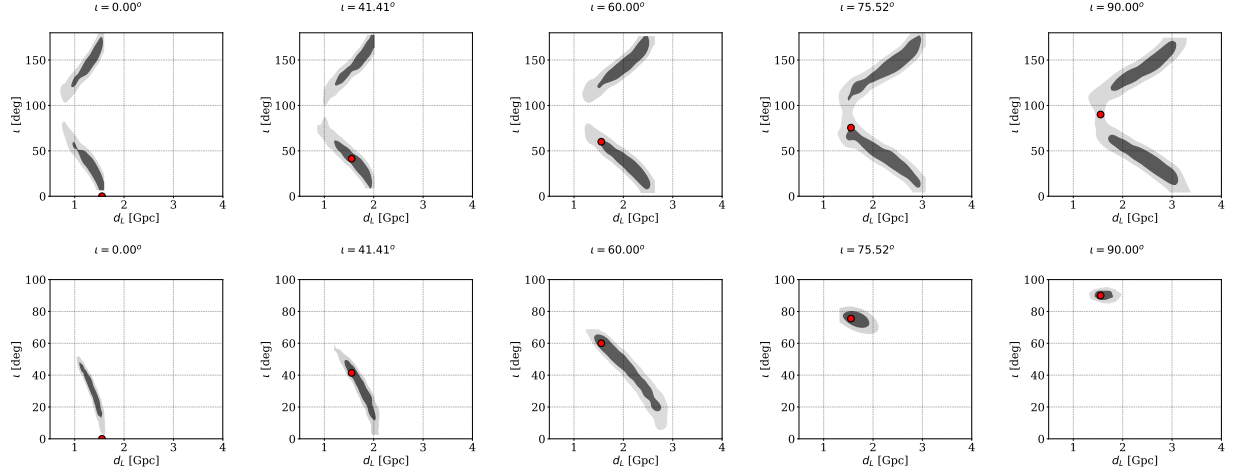


Figure 4: Examples of two-dimensional PDF for  $\iota$  vs.  $d_L$  for a single CE-like,  $L$ -shaped interferometer (top) and a triangle-shaped one (bottom) for source parameters giving  $\epsilon = 0.0089$  [73]. Note that the volumetric prior at recovery tends to disfavour  $\iota \rightarrow \pi/2$  for  $L$ -shaped detectors.

the polarisation dependent term to become equally important as the non- $\psi$  dependent term in (21). In turn, this leads to a better individuation of the polarisations, as exemplified by Figure 9. For  $z \sim 1$  detections disappear for the triangle-detector as they go below the  $SNR$  threshold, while this happens for the  $L$ -detector at larger distances because of its better sensitivity, see Figure 2.

For “tropical” inclination angles ( $\iota \sim \pi/2$ ) the  $\psi$ -dependent term is as important as the  $\psi$ -independent one, with the consequences that while for a  $L$ -shaped detector  $\psi$  cannot be constrained, for a triangle-shaped one a bimodality  $d_L$ - $\psi$  appears, see Figure 9.

Note that while it is more difficult for a CE-like detector to determine  $\iota$  than for a triangle one, Figure 7 shows that for specific cases CE can achieve a better precision due its better sensitivity, see Figure 2 and top line in Figure 8. Note that we used a volumetric prior on  $d_L$ , which tends to perform better for  $\iota \sim 0$ , but which can introduce bias for a  $L$ -shaped detector for “tropical”  $\iota$  (i.e.  $\iota \sim \pi$ ), as shown by the last top graph in Figure 4.



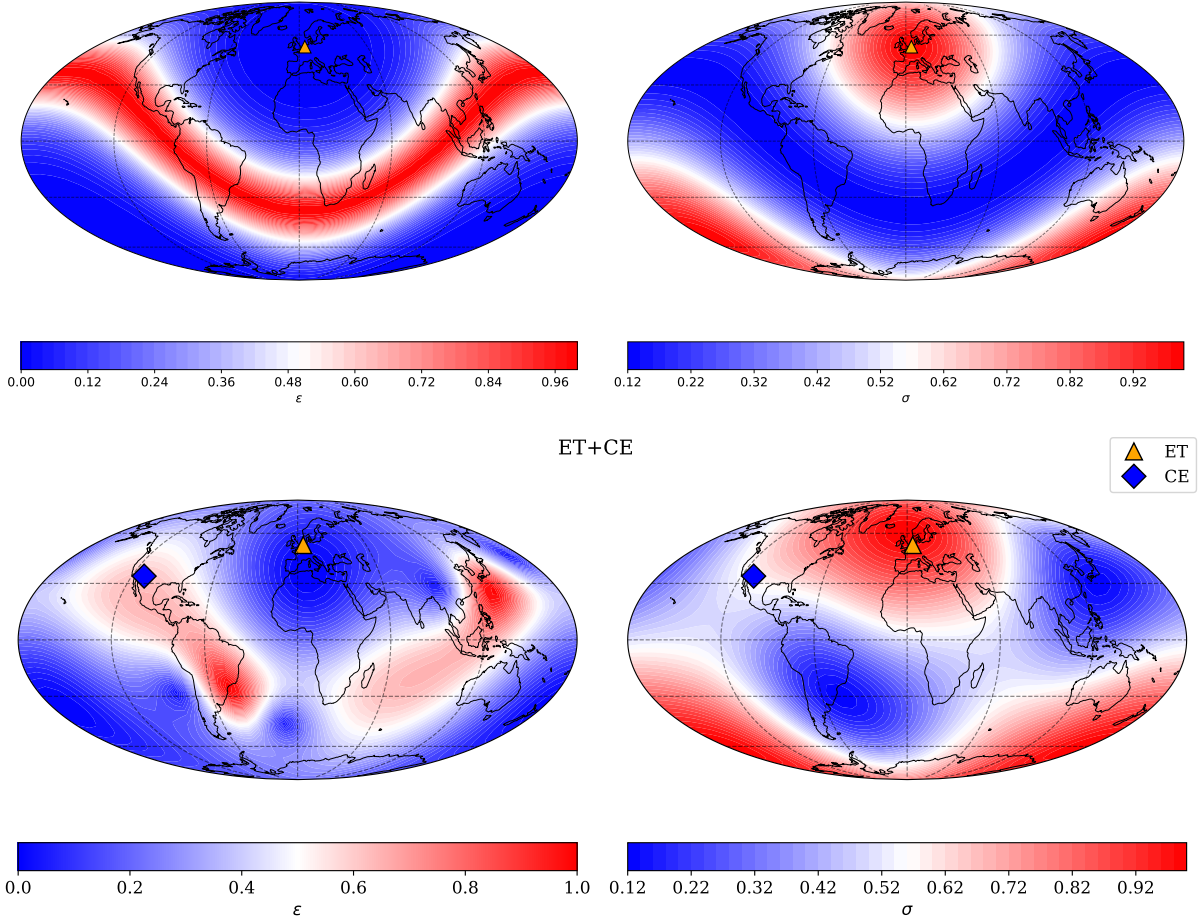


Figure 5: Values of  $\epsilon$  (left) and  $\sigma$  (right) for a single ET detector (top, ET location marked with a triangle) and for an ET-CE network (bottom, CE location marked with a diamond).

### C. Impact of detector relative orientation and localisation on $d_L$ uncertainty

#### 1. Two detectors

To investigate the best relative location and orientation of two detectors we place two CE-like detectors on the earth surface at an angular distance  $\Delta\theta$  one from the other and relative axis orientation  $\Delta\phi$ , with the result shown in the first three plots of Figure 11. The signals are simulated with three different distributions of inclination angles, all symmetric for  $\iota \rightarrow \pi - \iota$ , as reported in Figure 10 (dubbed *isotropic*, *smooth cutoff* and *hard cutoff*) corresponding to  $\hat{L}$  direction being isotropic in the 2-sphere, or to  $\iota$  values concentrated around 0 and  $\pi$ . Signals are produced for sources at three sample values of redshift:  $z = 0.1, 0.55, 1$

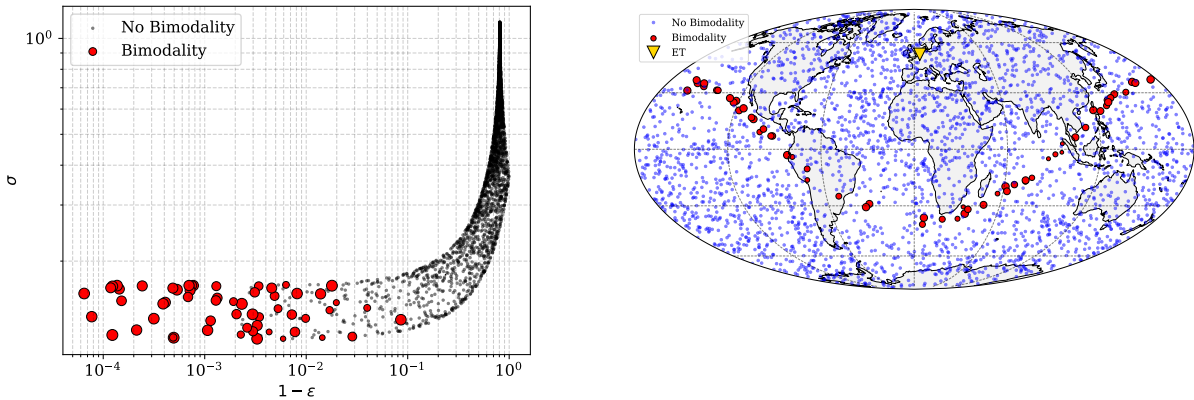


Figure 6: (Left) Distribution of  $\sigma$  and  $\epsilon$  values, defined in Equation (20), for a triangle-shaped interferometer. (Right) Points in the sky presenting bimodality are confined to the plane of the detector, where blind directions to individual interferometer appear. Operationally, we defined bimodality to be present when the ratio (smaller or equal to 1) of the height of the peaks of the  $\iota$  PDF is larger than the PDF value at  $\iota = \pi/2$ .

The lowest uncertainty is given by detectors either co-located or at antipodal sites, i.e. located on parallel planes, and at  $\Delta\phi = 45^\circ$  degree, so that such a network will have no blind spots, see Figure 11,12, which refers respectively to  $\iota$  of source distributed according to “smooth cutoff” or “isotropic” (there is no difference in the results between “smooth” and “hard cutoff”), and recovered in both cases with an isotropic prior in  $\iota$ .

In the same Figures 11,12 we also report the result of an analogue exercise with two ET-like detectors, suppressing the coordinate  $\Delta\phi$  that does not affect the result. In this case we find a moderate gain (a few percents) for angular separation  $\Delta\theta \simeq 40^\circ$  (or  $\Delta\theta \simeq 140^\circ$ ), which becomes more pronounced at larger redshift, where  $SNRs$  are smaller and uncertainties larger.

The differences between Figures 11 and 12 are minimal, showing that when the prior at recovery is isotropic in the inclination angle  $\iota$ , the injection distribution in  $\iota$  has little impact on  $d_L$  recovery precision.

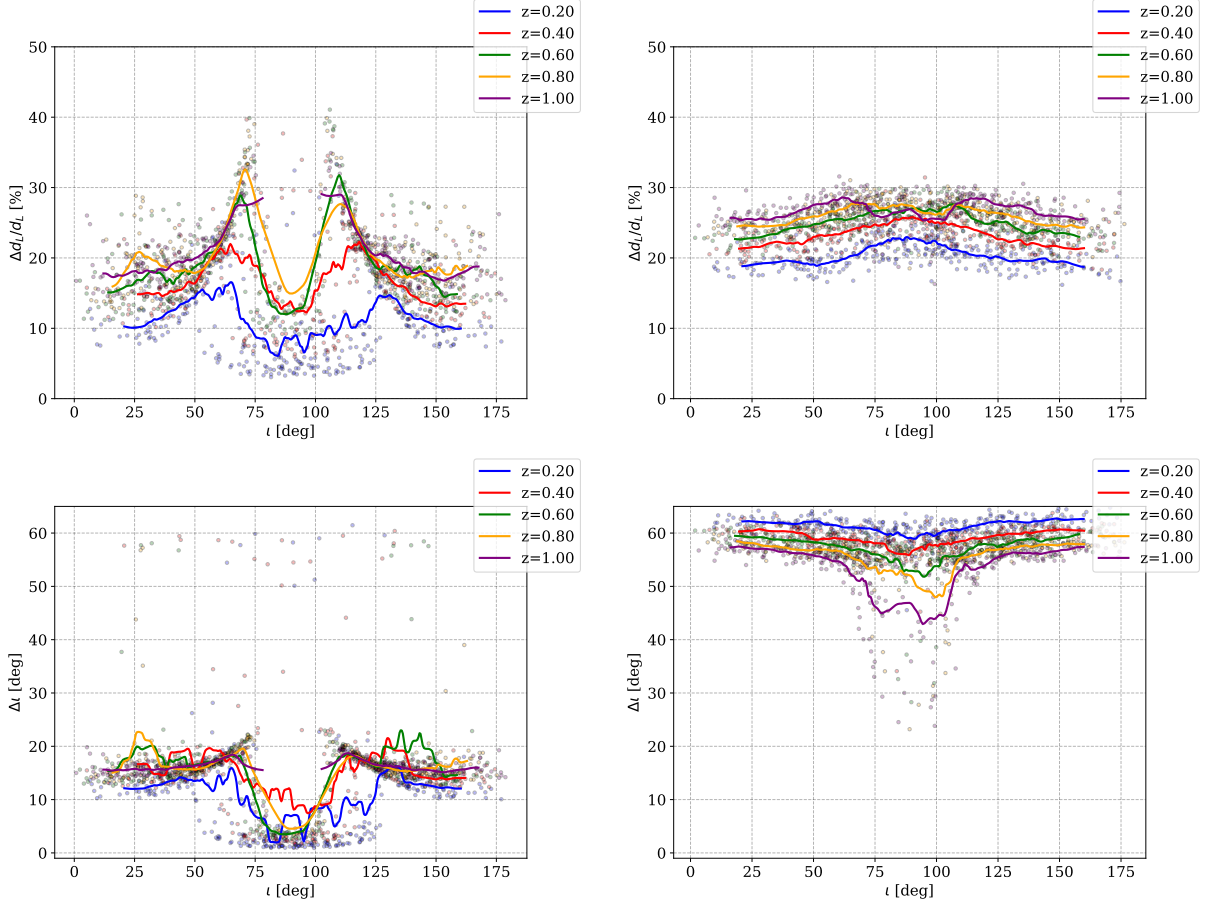


Figure 7: Scatter values and averages for relative uncertainty of  $d_L$  (top) and absolute one of  $\iota$  (bottom) as a function of  $\iota$  for various distances for an ET-like detector (left) and for a single CE one (right), for 300 simulations at each distance. Continuous lines are averages over intervals of 0.1 radians in  $\iota$ . Note the dip in  $d_L$  uncertainty for  $\iota \rightarrow \pi/2$  in the ET case. The points where CE outperforms ET in  $\Delta d_L$  are due to the better spectral noise sensitivity of the detector, see Figure 2, hence higher SNR, see Figure 8. Most of the recovered  $\iota$  for CE present bimodality ( $\Delta \iota \sim 60^\circ$ ), bimodality that happens far more rarely for ET, as shown by the red dots in the left plot of Figure 6 compared to the majority of gray points in the bottom right plot here clustering around  $\Delta \iota \sim 60^\circ$ . For ET-like detector there is no dip in  $d_L$  uncertainty for  $z \sim 1$  as the  $SNR$  decrease for  $\iota \rightarrow \pi/2$  moves the signal below the  $SNR = 8$  threshold, whereas for CE injections at  $z = 1$  are just above threshold.

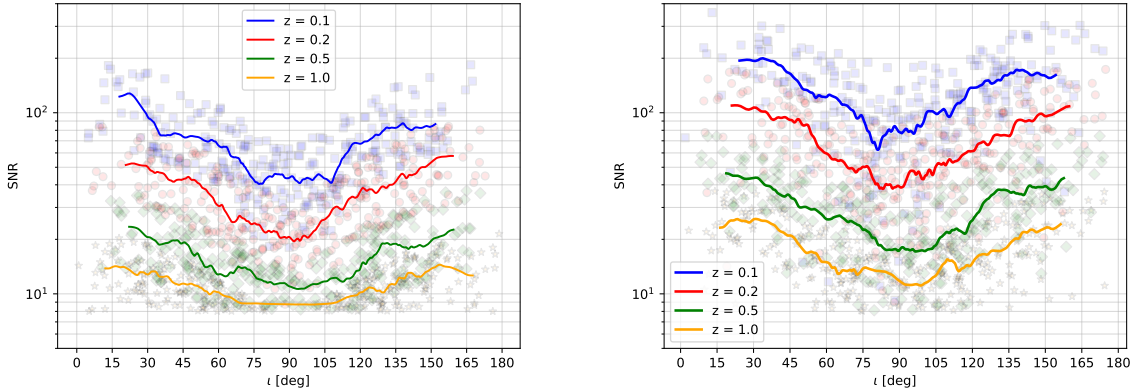


Figure 8:  $SNR$  as a function of  $\iota$  for various distances for a triangle interferometer (left) and for a single  $L$ -shaped detector (right).

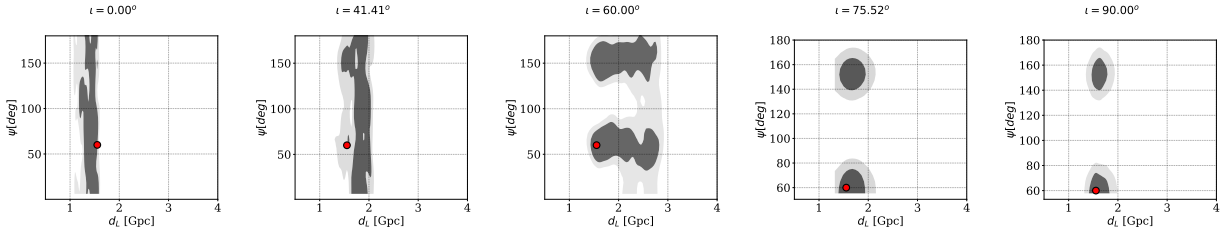


Figure 9: Examples of two-dimensional PDF for  $\psi$  vs.  $d_L$  for a single triangle-shaped interferometer showing that  $\psi$  determination accuracy improves as  $\iota \rightarrow \pi/2$ , as expected from Equation (21), whose  $\psi$ -dependent term is maximum for  $v = 1$ , which is  $\iota = \pi/2$ . The value for  $\epsilon$  is the same as in Figure 4.

## 2. Three detectors

Finally we fix the location of a ET-detector and a CE-one, corresponding to an angular distance of  $77^\circ$ . In this case we verified how the relative luminosity distance uncertainty averaged over source sky location varies with the position of a third ET-like detector, with results displayed in Figure 13 for redshift  $z = 0.1, 0.5, 1$ , showing overall a mild (sub-percent) dependence on the location of the third detector. When dealing with three detectors the relative measurement error on  $\Delta d_L$  depend very mildly on the source sky location, as shown by Figure 20.

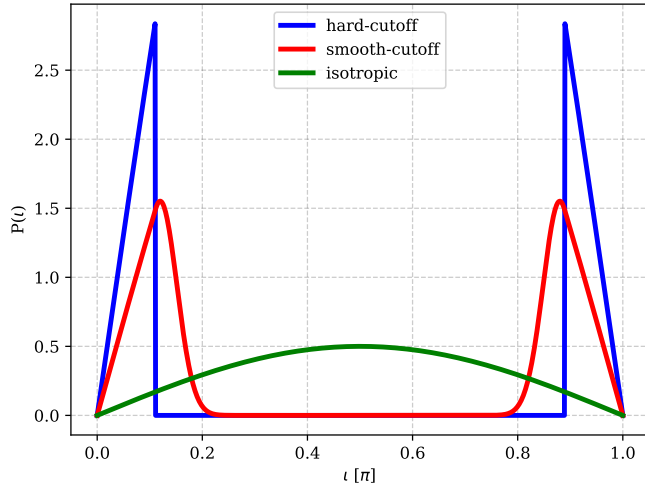


Figure 10: The three inclination angle distributions for  $\iota$  used in injections, dubbed “isotropic”, “smooth cutoff”, “hard cutoff”.

#### D. Impact of $\iota$ distribution and type of network on $d_L$ uncertainty

Beside the obvious importance of the number and quality of detectors in the network, another important feature in the forecast of luminosity distance uncertainty is the *source distribution of inclination angles*, for which we adopted the three distribution function in Figure 10.

Note that it is not a priori clear what distribution will be seen by 3G detector. While 2G ones are likely to see a distribution of small values for  $\min(\iota, \pi - \iota)$ , which give larger  $SNRs$ , since 3G detector will have a much larger reach, they should in principle see a distribution closer to the isotropic one, as observed in [76, 77]. However the selection of *bright* standard sirens may bias the observation towards GW signals accompanied by short GRB, which are expected to be somehow beamed [23] hence more likely to be observed for small  $\iota$  or  $\pi - \iota$ . On the other hand, short GRBs do not have good sky localisation, which can be achieved at high degree of accuracy with optical counterparts like kilonovae, that are broadly expected to be isotropically emitting [78], hence can support the expectation of a  $\sin \iota$ , isotropic distribution of sources.

We then summarize the result for the average  $d_L$  uncertainty for 6 different network of detectors: {ET, CE, CE+CE, ET+CE, ET+ET, ET+ET+CE} given the three different

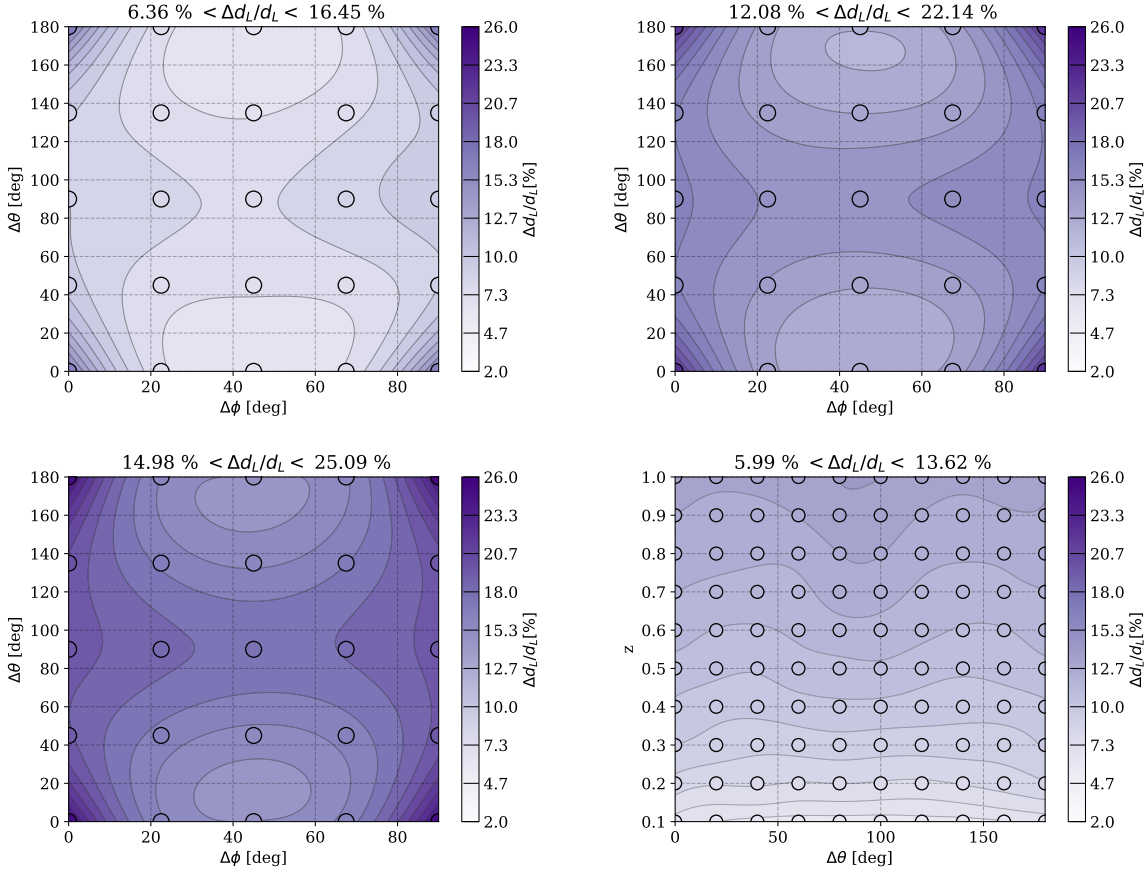


Figure 11: Error in distance determination averaged over source location, as a function of the angular distance between two 3G detectors. Sources are distributed isotropically in the sky before the  $SNR_i > 8$  cut in each detector. Source inclinations are distributed according to *smooth-cutoff* function, see Figure 10, Bayesian prior for  $\iota$  at recovery is isotropic. The bottom right plot refers to two ETs, the others to two CEs with sources respectively at  $z = 0.1, 0.55, 1$ .

$\iota$  source distributions. The  $\iota$  prior at recovery is chosen to be equal to the injected cutoff distribution in the top plot of Figure 14, and equal to an isotropic distribution in the bottom plot of the same Figure.

From Figure 14 we can draw interesting conclusions about the impact of the underlying inclination angle distributions and on the network features:

1. In the case GW sources are characterized by “polar” inclination angles, i.e. small values of either  $\iota$  or  $\pi - \iota$ , folding in such information at recovery leads to a significant improvement (up to a factor  $\sim 5$ ) in  $d_L$  uncertainty determination. This is shown by

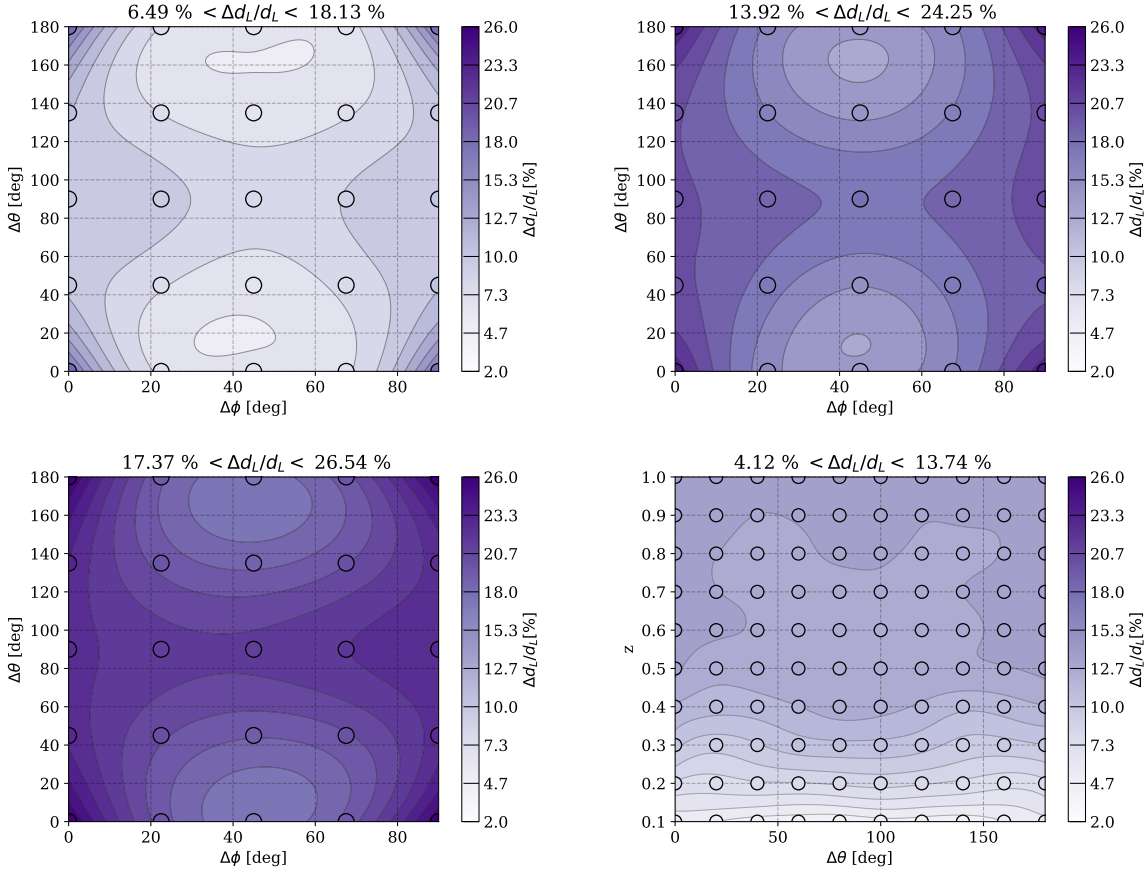


Figure 12: Same as in Figure 11 with source inclinations distributed isotropically on the 2-sphere.

the comparison of the two plots in Figure 14, where on the top plot results are shown for injections distributed at small angles only (see “hard-” and “smooth-cutoff” in Figure 10, using recovery prior equal to injection distribution), and the bottom plot has been obtained using an isotropic prior at recovery, i.e.  $\propto \sin \iota$ . In particular, in the top plot there is virtually no difference between the cases of hard- and smooth-cutoff, and also little difference between injections isotropic on the sphere or concentrated near the poles.

2. As expected, adding a 3G detectors to an existing network is beneficial to the  $d_L$  recovery precision, but less obvious is the effect of adding a CE-like detector instead of an ET-like one. A CE-CE network can ensure roughly the same precision as ET+ET+CE, and it is slightly better in terms of  $d_L$  precision than a ET+CE system, showing that the better design sensitivity we adopted for CE compared to ET, see left plot in Figure

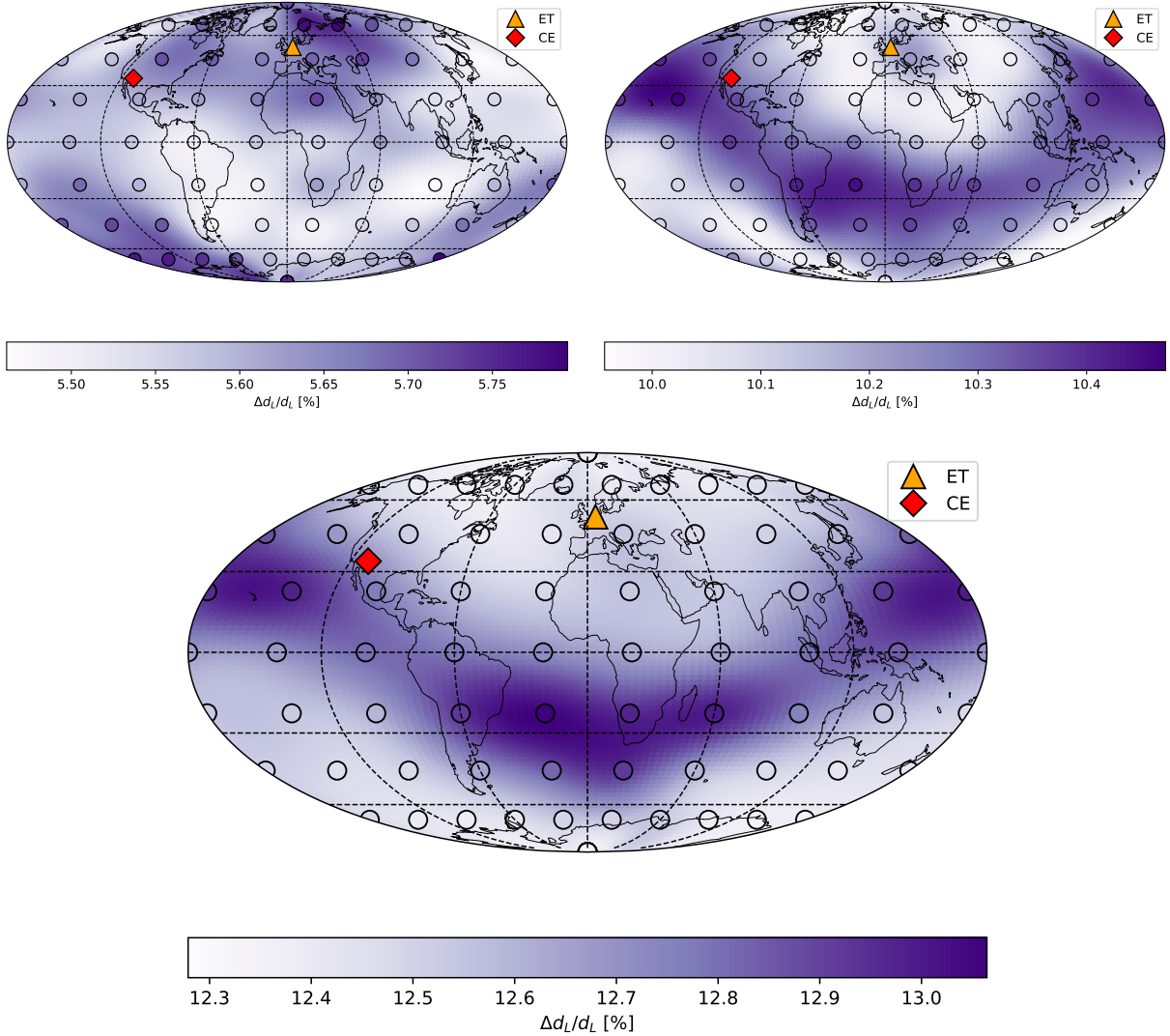


Figure 13: Luminosity distance uncertainty of a network of 3 detectors (ET+CE+ET) averaged over source location, depending on the location of the second ET-like detector. Empty circles denote the 90 trial location of the third detector, while the first ET and the CE detector are denoted respectively by a yellow triangle and red diamond. The three figures refer to redshift  $z = 0.1, 0.5, 1$ , respectively, moving clockwise from top left.

2, has a non-negligible effect when it comes to forming a network which has already good sky coverage, like e.g. a network of two  $L$ -shaped detectors.

For the dispersion of  $\Delta d_L/d_L$  values see Figure 19 in the 3 detector case of Figure 14.

Overall uncertainty in  $d_L$  smoothly increases with redshift, with results in broad agree-



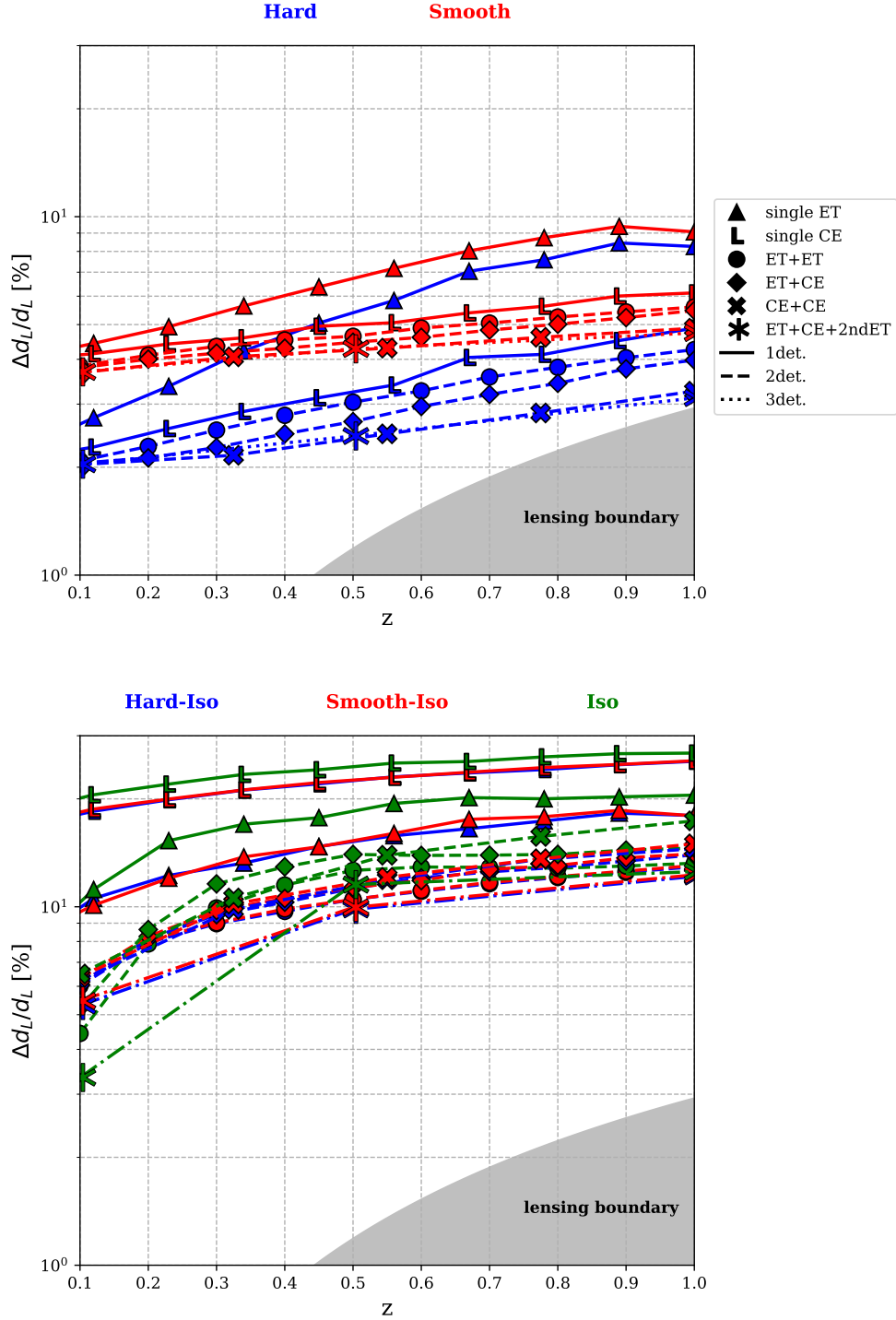


Figure 14: Average distance measure error for various network of ET- and CE-like detectors as a function of redshift. The top graph shows the case of anisotropic distribution of inclination angles with prior at recovery. The bottom one shows the case of isotropic prior at recovery for all cases of  $\iota$  injection distribution. See Figure 10 for  $\iota$  injection distributions (*Hard*, *Smooth*, *Iso*).

ment with the cumulative distributions shown in [53], see also [79] for binary black holes, even if a more detailed comparison is not possible as here, differently from there, we present results broken at specific redshift. For the reader interested in comparing with present observations, we report in Appendix D the same result of Figure 14 superimposed to scatter plots of luminosity distance uncertainties obtained with 2G detectors Advanced LIGO and Virgo in their first three observation runs [1–3], and with the *standard candle* catalogue [80].

Note that for a wide and sensitive enough detector network (ET+ET+CE) or CE+CE it is possible at moderately high redshift ( $\sim 0.7$ ) to almost reach the limit on  $d_L$  uncertainty imposed by the *lensing* intervening between source and observer, whose approximate value can be found in [81]. Also in [82] it is argued that with two or three 3G detectors working at design sensitivity it may be worth including de-lensing in the analysis of the signals, anticipating to 3G detectors what was foreseen for space interferometers [83]. Note while some present estimate indicate that having an EM counterpart of a GW detection may be challenging for source at redshift larger than  $\sim 0.7$  [37], there exist large uncertainties for the expected reach of next decades target-of-opportunity searches.

#### IV. CONCLUSIONS

With the goal of contributing to the use of gravitational wave signals from coalescing binaries as standard sirens to reconstruct the cosmic expansion history of the Universe, we analyzed the projected uncertainty measures of luminosity distances of third generation detectors. Observatories like the triangular Einstein Telescope, with arms at  $60^\circ$ , and the *L*-shaped Cosmic Explorer, with arms at  $90^\circ$ , are currently planned to start taking data just over a decade from now, but some of their features, like the exact location and topology, have not been finalized yet.

Luminosity distance precision measurement affects directly the measure of cosmological parameters, but luminosity distance correlates with a relatively large number of angular variables defining the relative location and orientation of source and detector. Such correlations can degrade the expected precision measurements, e.g. the one relying on Fisher matrix approximation, thus requiring a numerical Bayesian framework for a consistent analysis. For the sake of definiteness, we focused on bright standard sirens of binary neutron stars, for which a host galaxy can be identified and sky localization obtained with negligible

error, thus reducing the extrinsic angular variables to correlate with distance, to inclination, polarisation and phase-shift. We neglect arrival time and extrinsic parameters like masses which can be constrained with high accuracy from the GW phasing, and spins that are expected to be small for neutron star binaries giving rise to bright standard sirens.

We have neglected completely the effect of possible tidal deformation of neutron stars, which demand an accurate modelling of the waveform close to the merger, that is way beyond the scope of our work.

Our main results can be summarised as follows:

1. While the presence of bimodality in the luminosity distance ( $d_L$ ) versus inclination ( $\iota$ ) angle distribution is a well known feature of detections by single  $L$ -shaped interferometers, we have quantitatively linked such impossibility to separate individual polarisation contributions to a single scalar parameter, the  $\epsilon_D$  first introduced in [60] (simply  $\epsilon$  in this work). This parameter relates to the information of how much the sub-dominant polarisation is present in the combined detector output. In particular we have shown that detectors like the ones forming a triangular interferometer, which cover all sky localisations without blind directions, have  $\epsilon < 1$  for virtually all of the sky, and they can present bimodality in  $d_L$ - $\iota$  recovery only for specific directions with  $\epsilon \sim 1$ .
2. Another well-known feature of  $d_L$  vs.  $\iota$  uncertainty is the reduced error uncertainty for  $\iota \rightarrow \pi/2$  for triangular interferometers. We found that this is a generic feature ascribable to an improved precision in the determination of the *polarisation* angle, whose better constrained values are correlated with  $d_L$  measures.
3. We have shown quantitative measures of  $d_L$  uncertainties for a variety of networks made of up to three third generation detectors. Beside qualitative results presented in plots, we showed that given a network of at least two misaligned detectors, which then have virtually no blind spots in the sky, the best way to increase the precision measurement is to add a more sensitive detector, rather than adding an equally performing one, even if with more arms. Moreover we have shown that with three detectors one can almost reach the measurement error level set by lensing, which start to be at per-cent level from  $z \gtrsim 0.6$ .

4. We have quantified how the inclination angle distribution affect the  $d_L$  uncertainty measures, with the result that knowing the underlying  $\iota$  distribution can improve up to a factor 5 the luminosity distance uncertainty.

Obvious generalisations of the present work include to explore the non symmetric mass and spinning case. However, apart for the case of precessing binaries which however are not expected for bright standard sirens [84], this features are expected to induce quantitative, rather than qualitative changes of the results obtained here. One feature that could change the picture substantially is instead given by matter/tidal effect of neutron star, which are relevant close to the merger phase. Such effects are not only relevant for understanding the state of matter at high density inside the neutron stars, but have a non-trivial impact on cosmological parameter estimation, as they introduce into the phasing of the gravitational waveform a term that depends explicitly on redshift [34]. This would give a handle to estimate redshift with gravitational information alone, which however require accurate development of accurate and exhaustive matter waveforms, see e.g. [85] for a database.

### Appendix A: Polarisation angle

The radiation frame relative to the  $i$ -th detector is defined taking the  $\hat{z}_{rad}$  axis along the line pointing from the source to the observer ( $\hat{N}$ ) and the  $\hat{x}_{rad}$  axis in the  $\hat{z}_i$ - $\hat{z}_{rad}$  plane, being  $\hat{z}_i$  the unit vector normal to the plane of the detector, see Figure 3 for detector and radiation geometry.

The polarisation angle  $\psi_i$  is then conventionally defined as the angle from  $\hat{x}_{rad}$  to the line of *ascending nodes*, which is determined by the unit vector parallel to  $\hat{N} \times \hat{L}$ , being  $\hat{L}$  the unit vector parallel to the source angular momentum. One then has

$$\begin{aligned}\hat{x}_{i,rad} &\equiv \frac{\hat{z}_i - (\hat{z}_i \cdot \hat{N})\hat{N}}{|\hat{z}_i - (\hat{z}_i \cdot \hat{N})\hat{N}|}, \\ \hat{y}_{i,rad} &\equiv \hat{N} \times \hat{x}_{i,rad},\end{aligned}\tag{A1}$$

and

$$\begin{aligned}\cos \psi &= \hat{x}_{i,rad} \cdot \frac{\hat{N} \times \hat{L}}{|\hat{N} \times \hat{L}|}, \\ \sin \psi &= \hat{y}_{i,rad} \cdot \frac{\hat{N} \times \hat{L}}{|\hat{N} \times \hat{L}|},\end{aligned}\tag{A2}$$

from which it follows

$$\begin{aligned}\tan \psi_i &= \frac{(\hat{N} \times \hat{z}_i) \cdot (\hat{N} \times \hat{L})}{\hat{L} \cdot \left[ \hat{z}_i - \left( \hat{z}_i \cdot \hat{N} \right) \hat{N} \right]} \\ &= \frac{\hat{z}_i \cdot (\hat{N} \times \hat{L})}{\hat{z}_i \cdot (\hat{N} \times \hat{L})}.\end{aligned}\tag{A3}$$

In the specific case when  $\hat{L} \parallel \hat{N}$ , the polarisation angle  $\psi_i$  is not defined, as it is degenerate with a rotation in the plane of the orbit. The polarisation angle is also undefined if  $\hat{z} \parallel \hat{N}$ , in which case one cannot define the radiation triad.

Note that the angles  $\iota, \psi_i$ , with  $\cos \iota \equiv \hat{L} \cdot \hat{N}$ , determine the polar angles of  $\hat{L}$ , whose explicit components in the reference frame where  $\hat{N} \parallel \hat{z}$  and  $\hat{z}_i$  is in the  $\hat{x}$ - $\hat{z}$  plane, are:

$$\hat{L} = (\sin \iota \sin \psi_i, -\sin \iota \cos \psi_i, \cos \iota), \quad \hat{N} \parallel \hat{z}.\tag{A4}$$

We denote by  $\alpha, \beta$  the polar angles defining  $\hat{N}$ , ( $\alpha$  is the right ascension and the declination angle  $\delta$  is related to  $\beta$  via  $\delta = \pi/2 - \beta$ ) in the frame in which the reference vector  $\hat{z}_i = (0, 0, 1)$ :

$$\hat{N} = (\sin \beta \cos \alpha, \sin \beta \sin \alpha, \cos \beta), \quad \hat{z}_i \parallel \hat{z}.\tag{A5}$$

The transformation taking from the source frame to the radiation frame is  $R_z(\psi - \pi/2)R_y(\iota)R_z(\phi)$ , and the one taking  $\hat{N}$  from the form (A5) to the canonical form  $(0, 0, 1)$  is  $[R_z(\alpha)R_y(\beta)]^{-1}$ .

For a detector at latitude  $\lambda$  and longitude  $u$ , with  $\hat{N}$  given by Equation (A5), one has

$$\begin{aligned}\hat{z}_i &= (\cos \lambda \cos u, \cos \lambda \sin u, \sin \lambda), \\ \hat{x}_i &= (\cos \lambda \cos u - \cos \alpha \cos \beta \sin \lambda \sin \beta - \cos \lambda \cos(u - \alpha) \cos \alpha \sin^2 \beta, \\ &\quad \cos \lambda \sin u - \sin \alpha \cos \beta \sin \lambda \sin \beta - \cos \lambda \cos(u - \alpha) \sin \alpha \sin^2 \beta, \\ &\quad \sin \lambda \sin^2 \beta - \cos \lambda \cos(u - \alpha) \cos \beta \sin \beta) / \mathcal{N}, \\ \mathcal{N}^2 &\equiv 1 - [\cos \beta \sin \lambda + \cos \lambda \cos(u - \alpha) \sin \beta]^2,\end{aligned}\tag{A6}$$

and one can then find that  $\psi_i = \psi_0 + \delta\psi_i$  where  $\delta\psi_i$  is determined as

$$\begin{aligned}\mathcal{N} \cos \delta\psi_i &= \sin \lambda \sin \beta - \cos \lambda \cos(u - \alpha) \cos \beta, \\ \mathcal{N} \sin \delta\psi_i &= -\cos \lambda \sin(u - \alpha),\end{aligned}\tag{A7}$$

which shows that  $\delta\psi_i$  depends only on the location of the source and not on the reference polarisation angle  $\psi_0$ , as stated in Section II.

We conclude this Appendix by reporting the explicit expression of the angle  $\bar{\psi}$  defined in Equation (19):

$$\begin{aligned}\cos 4\bar{\psi} &= \frac{\Xi_{++} - \Xi_{\times\times}}{\Xi_0}, \\ \sin 4\bar{\psi} &= \frac{2\Xi_{+\times}}{\Xi_0}, \\ \Xi_0^2 &\equiv \Xi_{++}^2 + \Xi_{\times\times}^2 + 4\Xi_{+\times}^2 - 2\Xi_{++}\Xi_{\times\times},\end{aligned}\tag{A8}$$

and finally the relationship between  $\Xi_{dt_i AB}$  and its diagonal version (29)

$$\bar{\Xi}_{dt_i AB} = M_{AC}^{-1} \Xi_{dt_i CD} M_{DB},\tag{A9}$$

with

$$M_{AB} = \begin{pmatrix} \frac{F_+ \sin(2\psi_t) - F_\times \cos(2\psi_t)}{F_+ \cos(2\psi_t) + F_\times \sin(2\psi_t)} & \frac{F_+ \cos(2\psi) + F_\times \sin(2\psi)}{F_\times \cos(2\psi) - F_+ \sin(2\psi)} \\ 1 & 1 \end{pmatrix}.\tag{A10}$$

### Appendix B: Degeneracy between $d_L$ and $\iota$

According to the explanation given in Section II, see point 3 below Equation (21), the presence of bimodality is unavoidable (for  $\iota$  sufficiently distant from the value  $\pi/2$ ) for  $\epsilon \sim 1$ . Note that the blind zones of the individual interferometers making the ET are very close together, see Figure 15, so that for those specific source position the response of ET is not too dissimilar from the response of  $L$ -shaped detector.

Taking e.g. the case of 2G detectors, the two LIGOs are almost perfectly aligned, making  $\epsilon \sim 1$  for most of the sky, the addition of Virgo and KAGRA will not change drastically the situation as they have larger spectral noise sensitivity, see Figure 16 for the  $\sigma$  and  $\epsilon$  maps and Figure 17 for 2G detector design spectral noise sensitivities.

### Appendix C: Relation to dominant polarisation frame

In this work we relied on the parameterization leading to expression (21) that we borrowed from [60]. In [87] a similar parameterization has been introduced, identifying the *dominant polarisation frame*, i.e., the *radiation frame* for which the detector network is maximally sensitive to the + polarisation, by using the general property that different radiation frames

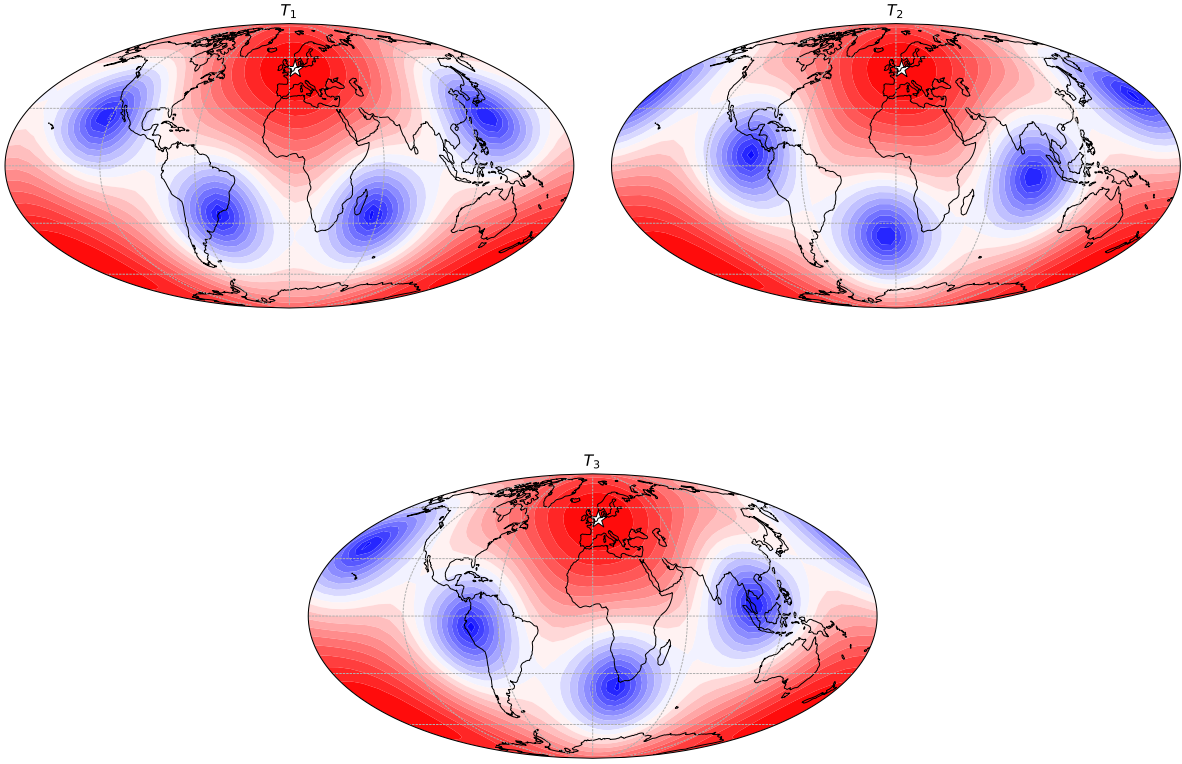


Figure 15: Quadratic sum of pattern function  $(f_+^2 + f_\times^2)^{1/2}$  for each of the three component of a triangular interferometer with arms at  $60^\circ$ . The blind spots of each individual iterferometer lie in the plane of the detector.

are related by a shift in the polarisation angle, i.e. a rotation around the propagation direction. The detector signal is then parameterized in [87] as

$$h_{det} = g_{Ref.[87]} (h_+ + \epsilon_{Ref.[87]} h_\times) , \quad (C1)$$

leading to the following mapping of these coefficients into our  $\sigma, \epsilon$  a

$$\begin{aligned} g_{Ref.[87]} &= \sigma \sqrt{1 + \epsilon} , \\ \epsilon_{Ref.[87]} &= \sqrt{\frac{1 - \epsilon}{1 + \epsilon}} . \end{aligned} \quad (C2)$$

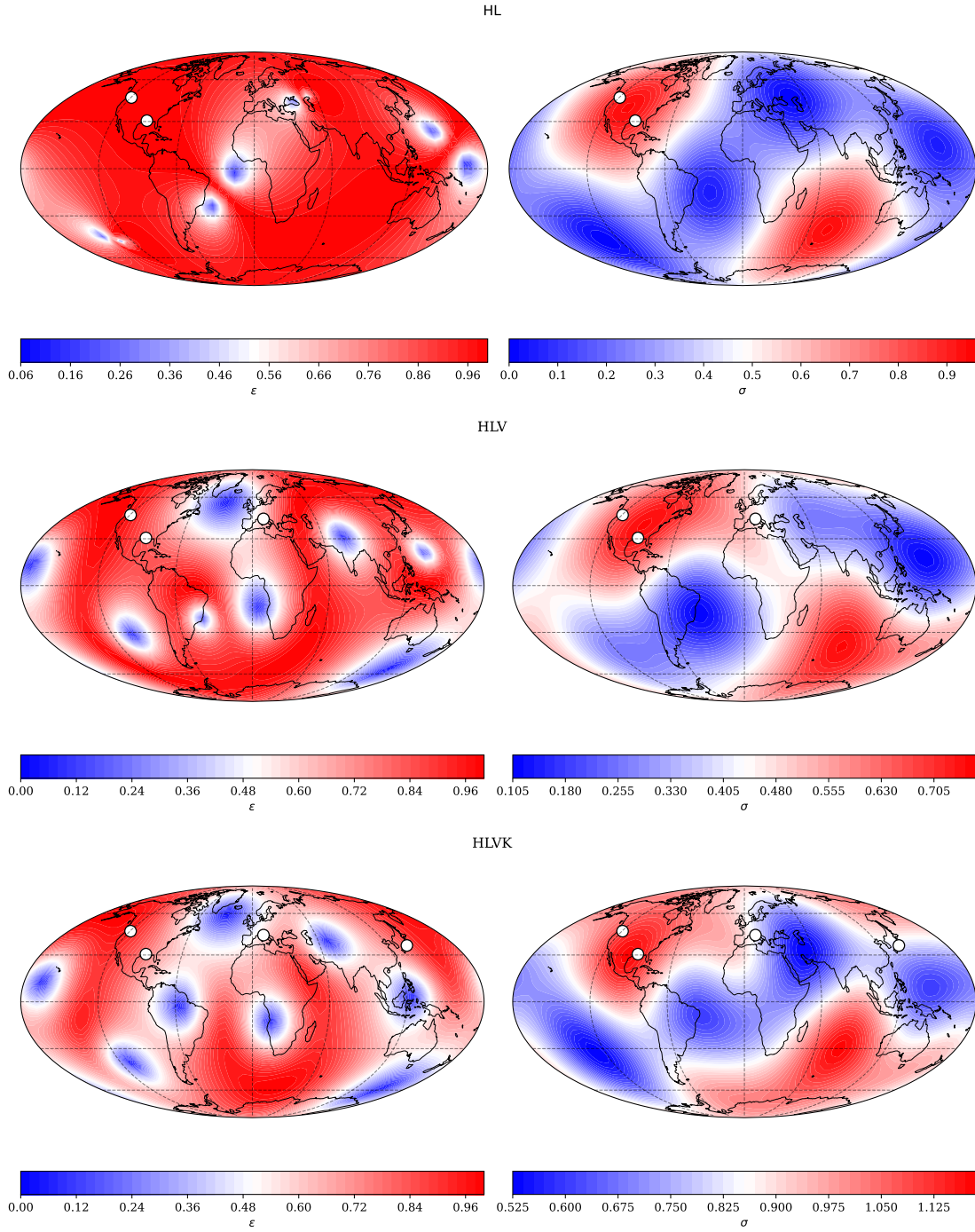


Figure 16: Values of  $\sigma$  and  $\epsilon$  for various networks of 2G detectors, spectral noise curves used are displayed in Figure 17.



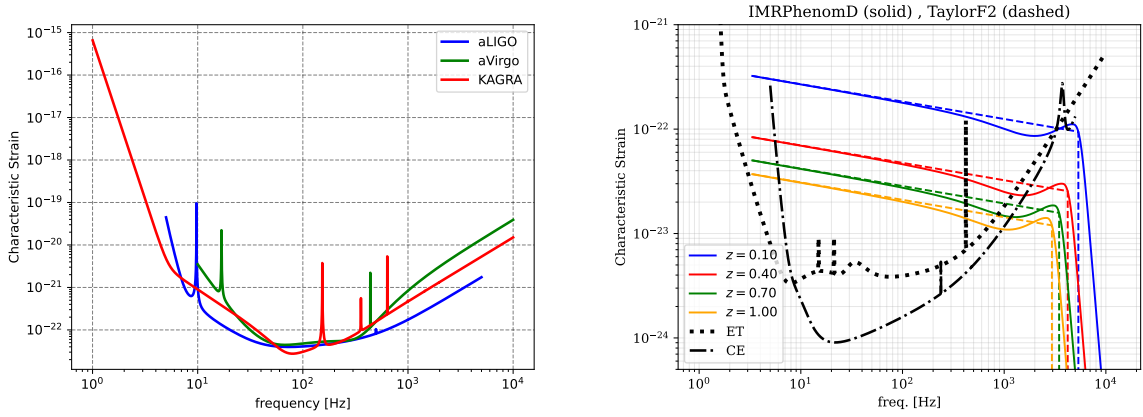


Figure 17: (Left) Characteristic strain  $\sqrt{f}S_n$  used to generate maps in Figure 16, from [86]. (Right) Examples of TaylorF2 (dashed) and IMRPhenomD (solid) waveforms for total mass  $3M_\odot$  and equal binary component masses.

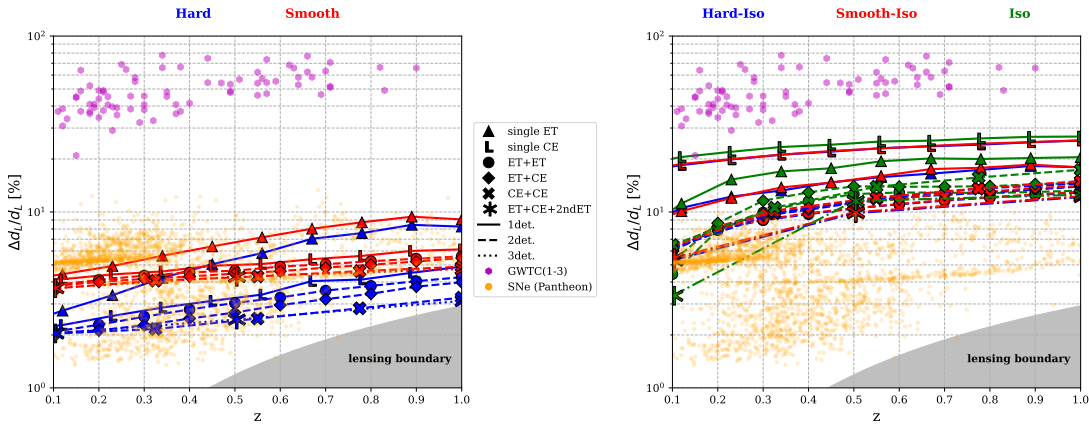


Figure 18: Same as in Figure 14, with uncertainties in luminosity distance of 2G detections from [1–3] and standard sirens from [80] added.

#### Appendix D: 3G luminosity distance uncertainty comparison with 2G detectors and standard candles

As a comparison with luminosity distance uncertainties obtained with 2G GW detectors and standard candles, we report in Figure 18 luminosity distance uncertainties from our 3G projections superimposed with the catalogues in [1–3] and [80].

Finally we report here the sky distribution of the injections used for the three detector

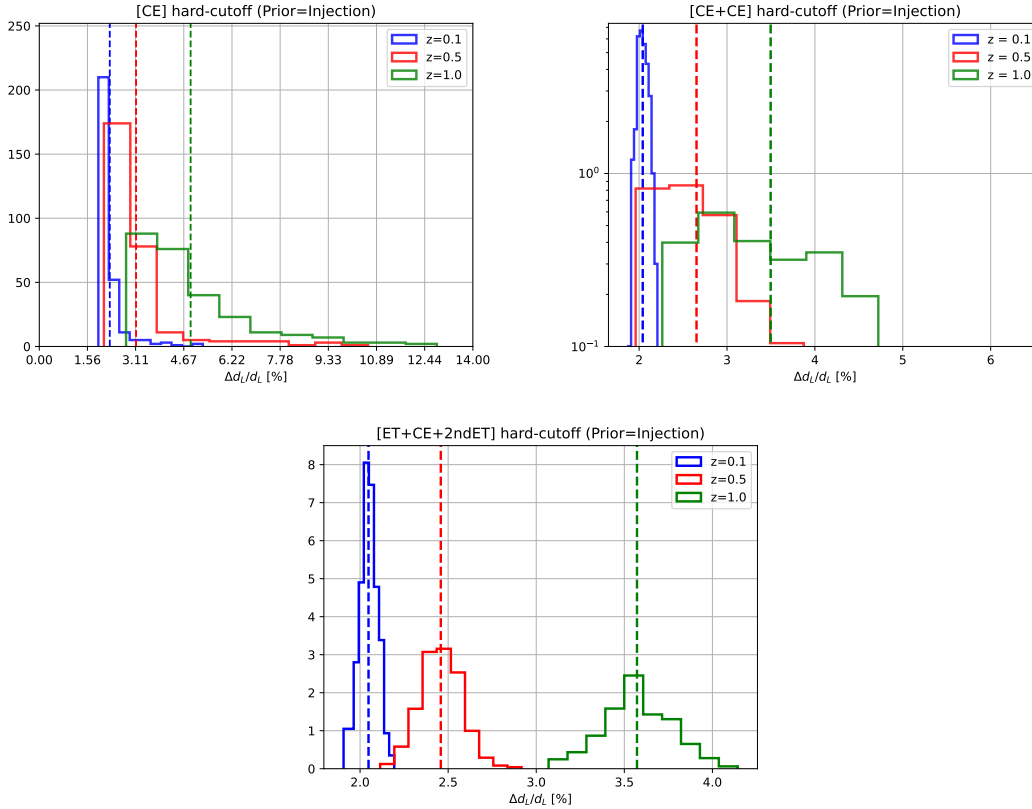


Figure 19: Histograms representing the dispersions of  $\Delta d_L/d_L$  measurements for sample 1,2 and 3 detector case case of Figures 14. *Hard-cutoff* refers to the  $\iota$  distributions of the injections as per Figure 10.

analysis of Section III C 2 (ET+CE+ET), which highlight the location selection effect of the SNR threshold at large distances.

### Acknowledgments

The authors thank Viviane Alfradique and Miguel Quartin for useful discussions. JMSdS is supported by the Coordenação de Aperfeiçoamento de Pessoal de Nível Superior (CAPES) – Graduate Research Fellowship/Code 001. The work of RS is partially supported by CNPq under grant 310165/2021-0 and by FAPESP grants 2021/14335-0 and 2022/06350-2. The authors thank the High Performance Computing Center (NPAD) at UFRN for providing

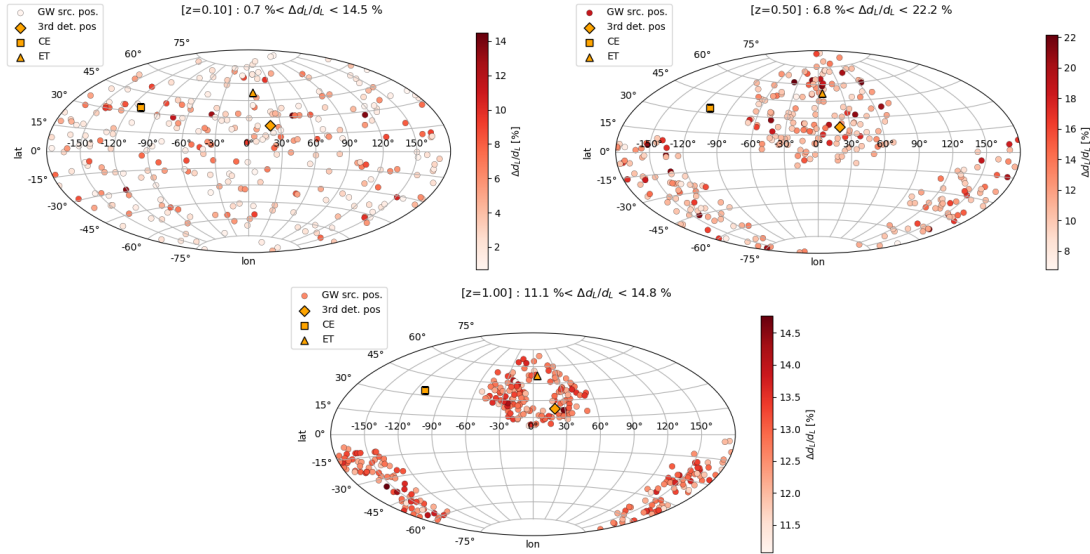


Figure 20: Sky distribution of above threshold events for the 3 detector network (ET+CE+ET) of Section III C 2, showing how threshold cut selects source sky regions.

computational resources that made the present work possible.

- 
- [1] B. P. Abbott et al. (LIGO Scientific, Virgo), *Phys. Rev. X* **9**, 031040 (2019), 1811.12907.
- [2] R. Abbott et al. (LIGO Scientific, Virgo), *Phys. Rev. X* **11**, 021053 (2021), 2010.14527.
- [3] R. Abbott et al. (LIGO Scientific, VIRGO, KAGRA) (2021), 2111.03606.
- [4] R. Abbott et al. (LIGO Scientific, Virgo), *Phys. Rev. D* **103**, 122002 (2021), 2010.14529.
- [5] R. Abbott et al. (LIGO Scientific, VIRGO, KAGRA) (2021), 2112.06861.
- [6] B. P. Abbott et al. (LIGO Scientific, Virgo, 1M2H, Dark Energy Camera GW-E, DES, DLT40, Las Cumbres Observatory, VINROUGE, MASTER), *Nature* **551**, 85 (2017), 1710.05835.
- [7] B. P. Abbott et al. (LIGO Scientific, Virgo, VIRGO), *Astrophys. J.* **909**, 218 (2021), 1908.06060.
- [8] R. Abbott et al. (LIGO Scientific, Virgo, KAGRA, VIRGO), *Astrophys. J.* **949**, 76 (2023), 2111.03604.
- [9] J. Aasi et al. (LIGO Scientific), *Class. Quant. Grav.* **32**, 074001 (2015), 1411.4547.
- [10] F. Acernese et al. (VIRGO), *Class. Quant. Grav.* **32**, 024001 (2015), 1408.3978.
- [11] B. P. Abbott et al. (KAGRA, LIGO Scientific, Virgo, VIRGO), *Living Rev. Rel.* **21**, 3 (2018),

1304.0670.

- [12] T. Akutsu et al. (KAGRA), *PTEP* **2021**, 05A101 (2021), 2005.05574.
- [13] B. F. Schutz, *Nature* **323**, 310 (1986).
- [14] D. E. Holz and S. A. Hughes, *Astrophys. J.* **629**, 15 (2005), astro-ph/0504616.
- [15] B. McKernan, K. E. S. Ford, W. Lyra, and H. B. Perets, *Monthly Notices of the Royal Astronomical Society* **425**, 460 (2012), ISSN 0035-8711, <https://academic.oup.com/mnras/article-pdf/425/1/460/3206708/425-1-460.pdf>, URL <https://doi.org/10.1111/j.1365-2966.2012.21486.x>.
- [16] I. Bartos, B. Kocsis, Z. Haiman, and S. Márka, *The Astrophysical Journal* **835**, 165 (2017), URL <https://dx.doi.org/10.3847/1538-4357/835/2/165>.
- [17] M. J. Graham, K. E. S. Ford, B. McKernan, N. P. Ross, D. Stern, K. Burdge, M. Coughlin, S. G. Djorgovski, A. J. Drake, D. Duev, et al., *Phys. Rev. Lett.* **124**, 251102 (2020), URL <https://link.aps.org/doi/10.1103/PhysRevLett.124.251102>.
- [18] B. McKernan, K. E. S. Ford, I. Bartos, M. J. Graham, W. Lyra, S. Marka, Z. Marka, N. P. Ross, D. Stern, and Y. Yang, *The Astrophysical Journal Letters* **884**, L50 (2019), URL <https://dx.doi.org/10.3847/2041-8213/ab4886>.
- [19] S. S. Kimura, K. Murase, and I. Bartos, *Astrophys. J.* **916**, 111 (2021), 2103.02461.
- [20] A. Palmese, M. Fishbach, C. J. Burke, J. T. Annis, and X. Liu, *Astrophys. J. Lett.* **914**, L34 (2021), 2103.16069.
- [21] W. E. East, L. Lehner, S. L. Liebling, and C. Palenzuela, *Astrophys. J. Lett.* **912**, L18 (2021), 2101.12214.
- [22] E. E. Flanagan and T. Hinderer, *Phys. Rev. D* **77**, 021502 (2008), 0709.1915.
- [23] B. D. Metzger and E. Berger, *Astrophys. J.* **746**, 48 (2012), 1108.6056.
- [24] G. Dály, G. Galgóczi, L. Dobos, Z. Frei, I. S. Heng, R. Macas, C. Messenger, P. Raffai, and R. S. de Souza, *Mon. Not. Roy. Astron. Soc.* **479**, 2374 (2018), 1804.05709.
- [25] B. P. Abbott et al. (LIGO Scientific, Virgo), *Phys. Rev. Lett.* **119**, 161101 (2017), 1710.05832.
- [26] W. Del Pozzo, *Phys. Rev. D* **86**, 043011 (2012), 1108.1317.
- [27] M. Soares-Santos et al. (DES, LIGO Scientific, Virgo), *Astrophys. J. Lett.* **876**, L7 (2019), 1901.01540.
- [28] R. Gray et al., *Phys. Rev. D* **101**, 122001 (2020), 1908.06050.
- [29] S. Mukherjee, B. D. Wandelt, S. M. Nissanke, and A. Silvestri, *Phys. Rev. D* **103**, 043520

- (2021), 2007.02943.
- [30] C. C. Diaz and S. Mukherjee, *Mon. Not. Roy. Astron. Soc.* **511**, 2782 (2022), 2107.12787.
- [31] L.-G. Zhu, Y.-M. Hu, H.-T. Wang, J.-d. Zhang, X.-D. Li, M. Hendry, and J. Mei, *Phys. Rev. Res.* **4**, 013247 (2022), 2104.11956.
- [32] H. Leandro, V. Marra, and R. Sturani, *Phys. Rev. D* **105**, 023523 (2022), 2109.07537.
- [33] J. M. Ezquiaga and D. E. Holz, *Astrophys. J. Lett.* **909**, L23 (2021), 2006.02211.
- [34] C. Messenger and J. Read, *Phys. Rev. Lett.* **108**, 091101 (2012), 1107.5725.
- [35] H.-Y. Chen, M. Fishbach, and D. E. Holz, *Nature* **562**, 545 (2018), 1712.06531.
- [36] T. Regimbau, M. Evans, N. Christensen, E. Katsavounidis, B. Sathyaprakash, and S. Vitale, *Phys. Rev. Lett.* **118**, 151105 (2017), 1611.08943.
- [37] E. Belgacem, Y. Dirian, S. Foffa, E. J. Howell, M. Maggiore, and T. Regimbau, *JCAP* **1908**, 015 (2019), 1907.01487.
- [38] J. M. S. de Souza, R. Sturani, and J. Alcaniz, *JCAP* **03**, 025 (2022), 2110.13316.
- [39] S. Vitale and C. Whittle, *Phys. Rev. D* **98**, 024029 (2018), 1804.07866.
- [40] P. Madau and M. Dickinson, *Ann. Rev. Astron. Astrophys.* **52**, 415 (2014), 1403.0007.
- [41] M. Punturo et al., *Class. Quant. Grav.* **27**, 194002 (2010).
- [42] M. Evans et al. (2021), 2109.09882.
- [43] M. Maggiore, *Gravitational Waves: Volume 1: Theory and Experiments*, Gravitational Waves (OUP Oxford, 2008), ISBN 9780198570745, URL <https://books.google.com.br/books?id=AqVpQgAACAAJ>.
- [44] H.-Y. Chen, D. E. Holz, J. Miller, M. Evans, S. Vitale, and J. Creighton, *Class. Quant. Grav.* **38**, 055010 (2021), 1709.08079.
- [45] V. Srivastava, D. Davis, K. Kuns, P. Landry, S. Ballmer, M. Evans, E. D. Hall, J. Read, and B. S. Sathyaprakash, *Astrophys. J.* **931**, 22 (2022), 2201.10668.
- [46] M. Evans, J. Jarms, and S. Vitale, Tech. Rep., LIGO Document P1600143, <https://dcc.ligo.org/LIGO-P1600143/public> (2016).
- [47] N. D. Lillo, A. Singha, A. Utina, and S. Hild, Tech. Rep., ET docs, <https://apps.et-gw.eu/tds/ql/?c=14313> (2019).
- [48] T. A. Apostolatos, C. Cutler, G. J. Sussman, and K. S. Thorne, *Phys. Rev. D* **49**, 6274 (1994).
- [49] L. Vainshtein and V. Zubakov, *Extraction of Signals from Noise: By L.A. Wainstein and V.D. Zubakov* (Dover, 1970), URL <https://books.google.com.br/books?id=PTPSzAEACAAJ>.

- [50] L. S. Finn and D. F. Chernoff, *Phys. Rev. D* **47**, 2198 (1993), gr-qc/9301003.
- [51] B. J. Owen, *Phys. Rev. D* **53**, 6749 (1996), gr-qc/9511032.
- [52] M. Burgay et al., *Nature* **426**, 531 (2003), astro-ph/0312071.
- [53] F. Iacovelli, M. Mancarella, S. Foffa, and M. Maggiore, *Astrophys. J.* **941**, 208 (2022), 2207.02771.
- [54] E. E. Flanagan and S. A. Hughes, *Phys. Rev. D* **57**, 4566 (1998), gr-qc/9710129.
- [55] B. Goncharov, A. H. Nitz, and J. Harms, *Phys. Rev. D* **105**, 122007 (2022), 2204.08533.
- [56] E. D. Hall and M. Evans, *Classical and Quantum Gravity* **36**, 225002 (2019), 1902.09485.
- [57] L. Sun et al., *Class. Quant. Grav.* **37**, 225008 (2020), 2005.02531.
- [58] B. Abbott et al. (LIGO Scientific), *Nucl. Instrum. Meth. A* **517**, 154 (2004), gr-qc/0308043.
- [59] V. Varma, P. Ajith, S. Husa, J. C. Bustillo, M. Hannam, and M. Pürrer, *Phys. Rev. D* **90**, 124004 (2014), 1409.2349.
- [60] C. Cutler and E. E. Flanagan, *Phys. Rev. D* **49**, 2658 (1994), gr-qc/9402014.
- [61] S. A. Usman, J. C. Mills, and S. Fairhurst, *Astrophys. J.* **877**, 82 (2019), 1809.10727.
- [62] S. Hild et al., *Class. Quant. Grav.* **28**, 094013 (2011), 1012.0908.
- [63] J. Veitch and W. Del Pozzo, *Tech. Rep.*, LIGO Document T1300326 (2013).
- [64] J. Veitch et al., *Phys. Rev. D* **91**, 042003 (2015), 1409.7215.
- [65] C. L. Rodriguez, B. Farr, V. Raymond, W. M. Farr, T. B. Littenberg, D. Fazi, and V. Kalogera, *Astrophys. J.* **784**, 119 (2014), 1309.3273.
- [66] G. Ashton et al., *Astrophys. J. Suppl.* **241**, 27 (2019), 1811.02042.
- [67] P. Mukherjee, D. Parkinson, and A. R. Liddle, *Astrophys. J. Lett.* **638**, L51 (2006), astro-ph/0508461.
- [68] J. Skilling, *Bayesian Analysis* **1**, 833 (2006).
- [69] B. S. Sathyaprakash and B. F. Schutz, *Living Rev. Rel.* **12**, 2 (2009), 0903.0338.
- [70] S. Husa, S. Khan, M. Hannam, M. Pürrer, F. Ohme, X. Jiménez Forteza, and A. Bohé, *Phys. Rev. D* **93**, 044006 (2016), 1508.07250.
- [71] S. Khan, S. Husa, M. Hannam, F. Ohme, M. Pürrer, X. Jiménez Forteza, and A. Bohé, *Phys. Rev. D* **93**, 044007 (2016), 1508.07253.
- [72] E. Chassande-Mottin, K. Leyde, S. Mastrogiovanni, and D. A. Steer, *Phys. Rev. D* **100**, 083514 (2019), 1906.02670.
- [73] V. Alfradique, M. Quartin, L. Amendola, T. Castro, and A. Toubiana, *Mon. Not. Roy. Astron.*

- Soc. **517**, 5449 (2022), 2205.14034.
- [74] S. Vitale and H.-Y. Chen, Phys. Rev. Lett. **121**, 021303 (2018), 1804.07337.
- [75] H.-Y. Chen, S. Vitale, and R. Narayan, Phys. Rev. X **9**, 031028 (2019), 1807.05226.
- [76] B. F. Schutz, Class. Quant. Grav. **28**, 125023 (2011), 1102.5421.
- [77] S. Vitale, Phys. Rev. D **94**, 121501 (2016), 1610.06914.
- [78] P. S. Cowperthwaite et al., Astrophys. J. Lett. **848**, L17 (2017), 1710.05840.
- [79] S. Vitale and M. Evans, Phys. Rev. D **95**, 064052 (2017), 1610.06917.
- [80] D. M. Scolnic et al. (Pan-STARRS1), Astrophys. J. **859**, 101 (2018), 1710.00845.
- [81] W. Zhao, C. Van Den Broeck, D. Baskaran, and T. Li, Phys. Rev. D **83**, 023005 (2011), 1009.0206.
- [82] X. Shan, C. Wei, and B. Hu, Mon. Not. Roy. Astron. Soc. **508**, 1253 (2021), 2012.08381.
- [83] N. Tamanini, C. Caprini, E. Barausse, A. Sesana, A. Klein, and A. Petiteau, JCAP **04**, 002 (2016), 1601.07112.
- [84] S. Vitale, R. Lynch, J. Veitch, V. Raymond, and R. Sturani, Phys. Rev. Lett. **112**, 251101 (2014), 1403.0129.
- [85] A. Gonzalez et al., Class. Quant. Grav. **40**, 085011 (2023), 2210.16366.
- [86] M. Evans, R. Sturani, S. Vitale, and E. Hall, Tech. Rep., LIGO DCC, <https://dcc.ligo.org/LIGO-T1500293/public> (2020).
- [87] S. Klimenko, S. Mohanty, M. Rakhmanov, and G. Mitselmakher, Phys. Rev. D **72**, 122002 (2005), gr-qc/0508068.